Magnetless Microwave Circulators Based on Spatiotemporally Modulated Rings of Coupled Resonators

Nicholas Aaron Estep, Dimitrios L. Sounas, *Member, IEEE*, and Andrea Alù, *Fellow, IEEE*

***Abstract*—Nonreciprocal components are ubiquitous in electronic and optical systems. To date, the use of magneto-optical materials has been the prevailing method to achieve nonreciprocity. However, magnetic-based devices are accompanied by several drawbacks, such as the requirement of bulky biasing devices and their incompatibility with semiconductor technology, which make their integration challenging. Recently, strong magnetless nonreciprocity was demonstrated in spatiotemporally modulated coupled-resonator networks as a result of an effective spin imparted to the structure by an RF signal. These structures can be easily integrated, and they potentially exhibit good power and noise performance, as any parametric device. Here, we develop an analytical theory for such devices, which allows determining the conditions for designing them with optimum characteristics, and present two designs based on lumped- and distributed-element circuits for applications at the very high-frequency and wireless-communications bands, respectively. The circulators exhibit large isolation and low insertion loss within reasonable modulation requirements. Furthermore, they can be realized with a modulation frequency substantially lower than the input frequency, significantly simplifying the design. Measurements for the lumped-element design are provided and show good agreement with theory and full-wave simulations. The nonlinear characteristics of the presented designs are also studied, and possible ways to reduce nonlinear distortion by increasing the static bias of the varactors or using advanced varactor topologies are explored.**

***Index Terms*—Circulator, nonreciprocity, temporal modulation.**

I. Introduction

IN ORDER to realize nonreciprocity, a crucial task in electronic and optical applications, one must break time-reversal symmetry. Nonreciprocal devices play a pivotal role in communication systems, from protecting coherent source generators from reflected signals, to cancelling crosstalk between transmit and receive signal paths in antenna feeding networks [1]. Onsager-Casimir's principle on reciprocity states that, in order to break the reciprocity of a linear system, it is necessary to bias it with a quantity that is odd-symmetric under time reversal [2]–[4]. Four quantities are known to satisfy this requirement, i.e., the magnetic field, the electric current, the linear momentum, and the angular momentum.

For decades, the most common approach for breaking reciprocity consisted in applying external magnetic fields to ferromagnetic media [1], [5]. In the absence of a magnetic field, the microscopic magnetic domains in such materials are oriented in random directions and the net magnetic activity is negligible. However, when biased with a static magnetic field [see Fig. 1(a)], these microscopic domains are aligned in the same direction (along the magnetic bias) and a preferred rotation direction is imparted to the corresponding magnetic moments. As a result, circularly polarized electromagnetic waves with opposite rotation directions interact differently with such media, and time-reversal symmetry (reciprocity) is broken. Magnetic biasing may provide a well-established means to break reciprocity, but contains innate limitations. Integration of magnetic materials into complementary metal–oxide–semiconductor (CMOS) processing is a challenging task, due to

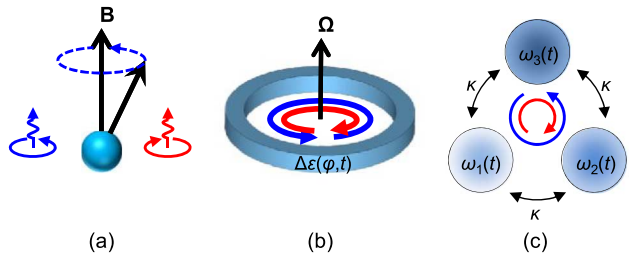

Fig. 1. Nonreciprocity through biasing with magnetic and angular-momentum vectors. (a) Magnetic nonreciprocity. When a ferromagnetic medium is biased with static magnetic field, the electrons of the medium precess preferably in a particular direction. As a result, circularly polarized waves with opposite rotation directions interact differently with the medium (their effective refractive indices are different) and nonreciprocity is produced. (b) Angular-momentum nonreciprocity with a resonant ring. By imparting angular momentum to the ring, either mechanically or electrically, we can lift the degeneracy between counter-rotating modes of the ring and produce nonreciprocity. (c) Angular-momentum nonreciprocity with a loop of identical resonators symmetrically coupled to each other. Angular momentum is effectively applied to the loop by modulating the resonators with low-frequency signals with equal amplitudes and phase difference of 120°. Modulation lifts the degeneracy of the counter-rotating modes of the *loop*, as opposed to the counter-rotating states of a *single ring* in (b).

Manuscript received July 17, 2015; revised November 25, 2015 and December 18, 2015; accepted December 19, 2015. This work was supported by the Air Force Office of Scientific Research under Grant FA9550-14-1-0105 and Grant FA9550-13-1-0204, by the National Science Foundation under Grant ECCS-1406235, and by the Defense Threat Reduction Agency under Grant HDTRA1-12-1-0022. Author A. Alù acts as Chief Technology Officer of Silicon Audio RF Circulator, LLC. The terms of this arrangement have been reviewed and approved by The University of Texas at Austin in accordance with its policy on objectivity in research.

The authors are with the Department of Electrical and Computer Engineering, The University of Texas at Austin, Austin, TX 78712 USA (e-mail: alu@mail.utexas.edu).

Color versions of one or more of the figures in this paper are available online at http://ieeexplore.ieee.org.

Digital Object Identifier 10.1109/TMTT.2015.2511737

the incompatibility between magnetic materials and semiconductors in terms of their crystal structure [6], and the typical requirement of external biasing devices, which increase size and weight. External biasing may be avoided through ferromagnetic materials with spontaneous magnetization, such as hexaferrites [7] and ferromagnetic nanowire membranes [8], [9], but such approaches are currently limited by fabrication challenges and the nonoptimal performance of the corresponding devices. On the other hand, the integration of nonreciprocal devices is of tremendous importance since it may eventually allow the realization of full-duplex communication systems and enhance the speed of wireless communications networks.

Several alternatives to magnetic biasing were proposed in the past decades, the first one involving circuits with field-effect transistors [10], [11]. Such approaches are fully compatible with integrated circuit (IC) technology, but they generally suffer from poor noise performance and strong nonlinearity. More recently, [12]–[14] proposed a class of magnetless nonreciprocal metamaterials based on transistor-loaded rings. Transistors force waves in the rings to travel in only one direction, thereby mimicking the electron spin precession in magnetized ferrites. These works were successful in realizing effective ferrite media, which, like real ferrites, can produce Faraday rotation or be used as substrates in microwave devices. However, they are also bound to the limitations related to power handling, nonlinearities, and noise sensitivity of previous transistor-based approaches. Transistor-based metamaterials were also presented in [15] and [16], with similar limitations. Nonlinearity was also studied as a potential path to magnetless nonreciprocity, especially at optical frequencies [17]–[20]. However, such approaches usually require strong input intensities and lead to significant signal distortion, in addition to being inherently dependent on the signal amplitude.

Following an approach similar to distributed parametric amplification and frequency conversion [21]–[24], it was recently shown that linear low-noise strong nonreciprocity can be achieved by spatiotemporal modulation of waveguides via appropriate electrical or acoustical signals [25]–[34]. However, the weak nature of the electro-optical and acousto-optical effects, through which modulation is typically achieved, leads to bulky devices, especially at optical frequencies. Furthermore, many of these works rely on nonuniform modulation across the waveguide cross section, significantly complicating the fabrication process.

Inspired by Onsager-Casimir's principle and the physical mechanism that creates nonreciprocity in ferrites, [35] presented a new class of metamaterials that provide strong, low-noise, and linear nonreciprocity at the sub-wavelength scale through biasing with the angular-momentum vector. The main element of these metamaterials is a ring resonator, which, like the atoms of real materials, supports pairs of degenerate states with opposite angular momentum. Biasing the ring with the angular momentum vector lifts the degeneracy and produces nonreciprocity, much like a magnetic bias produces nonreciprocity in ferromagnetic materials [see Fig. 1(b)]. This concept was experimentally proven in acoustics by circulating air in a ring resonator, thereby demonstrating the first-ever acoustic circulator [36].

Since physical rotation is obviously impractical for electromagnetic devices, [35] proposed to realize effective electric rotation through appropriate spatiotemporal modulation. In particular, it was shown that the degeneracy of the lth order modes of a ring (modes with azimuthal variation $e^{\pm il\varphi}$) can be lifted by modulating the permittivity of the ring as $\Delta\varepsilon(\varphi,t) = \Delta\varepsilon_{\rm m}\cos(\omega_{\rm m}t - l_{\rm m}\varphi)$, where $\Delta\varepsilon_{\rm m}$, $\omega_{\rm m}$, and $l_{\rm m} = 2l$ represent the perturbation of the ring permittivity, the modulation frequency, and the modulation azimuthal order, respectively. Such permittivity modulation leads to an effective rotation with angular velocity $\Omega_{\rm m} = \omega_{\rm m}/l_{\rm m}$. Contrary to the approaches of [25], [28], and [29], the modulation in [35] is continuous across the transverse surface area of the ring, significantly relaxing manufacturing requirements. In addition, the use of a ring resonator significantly boosts the otherwise weak modulation effect, resulting in strong nonreciprocity at the sub-wavelength scale.

In practice, the modulation of the ring needs to be implemented in a discrete fashion via a number of different regions with uniform modulation [37]. Such a discretization results in a reduction of the modulation efficiency by a factor of $\mathrm{sinc}(2l/N)$ for N modulation regions, where $\mathrm{sinc}x = \sin(\pi x)/x$, revealing a tradeoff between performance and fabrication complexity. To avoid this problem, [38] introduced a new design based on three identical resonators symmetrically coupled to each other and modulated by signals with the same amplitude and phase difference of 120° [see Fig. 1(c)]. In this particular design, nonreciprocity is the result of lifting the degeneracy of the counter-rotating modes of the *composite loop*, as opposed to lifting the degeneracy of the modes of a single ring, as in [35]. Since the modulation of each resonator in the loop is uniform, the modulation efficiency of this structure can reach 100%.

The design in [38] was based on a heuristic empirical approach and, although it provided large isolation, it exhibited poor performance in terms of insertion loss and intermodulation products. Similar designs were also presented in [39] with the same limitations. Here, by using coupled-mode theory (CMT), we develop an analytical theory for circulators based on loops of modulated resonators, which allows designing such devices with optimum performance in terms of isolation, insertion loss, and intermodulation products, for given quality factors of their constituent elements and specified modulation parameters. This theory is used to design two circulators, for the very high-frequency (VHF) and wireless-communications bands, with significantly improved characteristics with respect to the preliminary designs in [38] and [39]. The designs are based on the wye resonator topology, which was first introduced in [40] for overcoming the performance issues and implementation challenges of the designs in [38] and [39]. The design in [40] was based on a heuristic nonrigorous approach and, as a result, it was nonoptimal. Furthermore, no experimental proof was included in [40]. Here, we apply the results of CMT to the wye topology in [40] in order to design an optimal lumped-element circulator for the VHF band with commercially available components. Measurements are provided and shown to be in very good agreement with CMT and full-wave simulations. A new distributed-element design is also introduced, for applications at the wireless-communications band. Finally, we study the nonlinear proper-

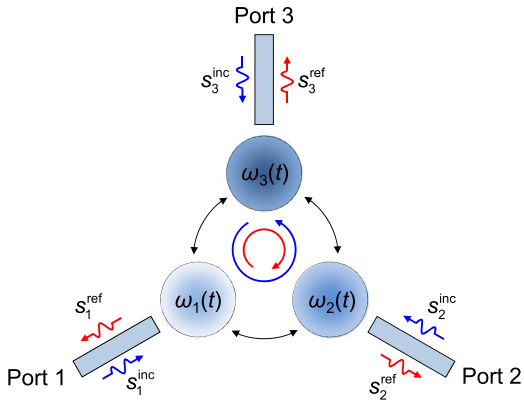

Fig. 2. Circulator based on a spatiotemporally modulated loop of coupled resonators, where the resonators are additionally coupled to external transmission lines.

ties of both designs and discuss possible approaches for improving them.

This paper is organized as follows. Section II presents the coupled-mode analysis for the most general form of the proposed devices. Section III presents the lumped- and distributed-element designs, including experimental results for the lumped-element design. Finally, conclusions are provided in Section IV. The analysis in this paper follows the $e^{-i\omega t}$ harmonic convention and simulations are performed with CST Microwave Studio and Advanced Design Studio.

II. Theory

A. Coupled-Mode Equations

Fig. 2 illustrates the most general form of a circulator based on a loop of modulated resonators: it consists of three identical modulated resonators, as described previously, symmetrically coupled to three transmission lines. Networks of coupled resonators can be efficiently studied via CMT [41], which, when applied to the network in Fig. 2, yields

$$\begin{aligned}\dot{\mathbf{a}} &= (-i\boldsymbol{\Omega} - \boldsymbol{\Gamma})\mathbf{a} + \mathbf{D}^{\mathrm{T}}\mathbf{s}^{\mathrm{inc}} \\ \mathbf{s}^{\mathrm{ref}} &= \mathbf{C}\mathbf{s}^{\mathrm{inc}} + \mathbf{D}\mathbf{a}.\end{aligned} \tag{1}$$

In the above equation, $\mathbf{a} = (a_1\ a_2\ a_3)^{\mathrm{T}}$ is the state vector, with a_i the field amplitude at the ith resonator, $\mathbf{s}^{\mathrm{inc}} = (s_1^{\mathrm{inc}}\ s_2^{\mathrm{inc}}\ s_3^{\mathrm{inc}})^{\mathrm{T}}$ is the incident-signal vector with s_i^{inc} being the incident signal at the ith transmission line, and $\mathbf{s}^{\mathrm{ref}} = (s_1^{\mathrm{ref}}\ s_2^{\mathrm{ref}}\ s_3^{\mathrm{ref}})^{\mathrm{T}}$ being the reflected-signal vector, with s_i^{ref} being the reflected signal at the ith transmission line. The state vector is normalized so that $|\mathbf{a}|^2$ represents the stored energy in the system. Furthermore, $\boldsymbol{\Omega}$ is the system frequency matrix, which incorporates the resonance frequencies and cross-coupling between the resonators, $\boldsymbol{\Gamma}$ is the system decay matrix, which incorporates the decay mechanisms of the system, $\mathbf{D}$ is a matrix describing coupling between the lines and the resonators, and $\mathbf{C}$ is a matrix describing immediate coupling between the lines. Explicit expressions for these matrices will be provided in the following.

Since the network in Fig. 2 consists of identical resonators with symmetrical coupling between them, $\boldsymbol{\Omega}$, $\boldsymbol{\Gamma}$, and $\mathbf{D}$ need to be symmetrical as well,

$$\begin{aligned}\boldsymbol{\Omega} &= \begin{pmatrix}\omega_0 & \kappa & \kappa \\ \kappa & \omega_0 & \kappa \\ \kappa & \kappa & \omega_0\end{pmatrix} \\ \boldsymbol{\Gamma} &= \begin{pmatrix}\gamma & \zeta & \zeta \\ \zeta & \gamma & \zeta \\ \zeta & \zeta & \gamma\end{pmatrix} \\ \mathbf{D} &= \begin{pmatrix}d & g & g \\ g & d & g \\ g & g & d\end{pmatrix}.\end{aligned} \tag{2}$$

The diagonal elements of these matrices refer to isolated resonators, while the off-diagonal elements describe the effect of coupling. In general, $\boldsymbol{\Gamma}$ consists of two parts, $\boldsymbol{\Gamma}_{\mathrm{loss}}$ and $\boldsymbol{\Gamma}_{\mathrm{cpl}}$, corresponding to the intrinsic loss of the resonators and leakage to the external lines, respectively. The matrices $\boldsymbol{\Gamma}_{\mathrm{cpl}}$, $\mathbf{D}$, and $\mathbf{C}$ should satisfy the general CMT conditions

$$\begin{aligned}\mathbf{D}^{\mathrm{H}}\mathbf{D} &= 2\boldsymbol{\Gamma}_{\mathrm{cpl}} \\ \mathbf{C}\mathbf{D}^{*} &= -\mathbf{D}\end{aligned} \tag{3}$$

resulting from power conservation and time-reversal symmetry. The matrix $\mathbf{C}$ is essentially the scattering matrix of the system for frequencies far from the system resonances, when $\mathbf{a} \approx 0$. If the coupling between ports is only achieved through the resonators, as for all the structures presented here, coupling between different ports is negligible for frequencies far from the system resonances and $\mathbf{C}$ is a diagonal matrix. Based on this fact and selecting the reference planes of the external lines so that the diagonal elements of $\mathbf{D}$ are real, (3) lead to $\mathbf{C} = -\mathbf{I}_3$, where $\mathbf{I}_3$ is the 3×3 identity matrix.

Modulation is applied to the resonators so that their resonance frequencies vary in time according to $\omega_1(t) = \omega_0 + \delta\omega_{\mathrm{m}}\cos(\omega_{\mathrm{m}}t)$, $\omega_2(t) = \omega_0 + \delta\omega_{\mathrm{m}}\cos(\omega_{\mathrm{m}}t + 2\pi/3)$, and $\omega_3(t) = \omega_0 + \delta\omega_{\mathrm{m}}\cos(\omega_{\mathrm{m}}t + 4\pi/3)$, where ω_0 is the resonance frequency of the nonmodulated resonators, $\delta\omega_{\mathrm{m}}$ is the magnitude of the resonance-frequency perturbation, and ω_{m} is the modulation frequency. This form of modulation imparts an effective electric rotation to the loop of coupled resonators, as discussed in Section I. Then, $\boldsymbol{\Omega} = \boldsymbol{\Omega}_0 + \delta\boldsymbol{\Omega}_{\mathrm{m}}$, where $\boldsymbol{\Omega}_0$ is the static part of the modulation matrix, as given in (2) (the part corresponding to the system without modulation) and

$$\begin{aligned}&\delta\boldsymbol{\Omega}_{\mathrm{m}} \\ &= \delta\omega_{\mathrm{m}}\begin{pmatrix}\cos(\omega_{\mathrm{m}}t) & 0 & 0 \\ 0 & \cos(\omega_{\mathrm{m}}t + 2\pi/3) & 0 \\ 0 & 0 & \cos(\omega_{\mathrm{m}}t + 4\pi/3)\end{pmatrix}.\end{aligned} \tag{4}$$

Since the applied weak modulation is simply a perturbation of the static (nonmodulated) loop, it is convenient to express (1) in the eigenbasis of the static loop (eigenbasis of $\boldsymbol{\Omega}_0$), which consists of a common state, with frequency $\omega_{\mathrm{c}} = \omega_0 - 2\kappa$ and state vector $\mathbf{a}_{\mathrm{c}} = (1\ 1\ 1)^{\mathrm{T}}/\sqrt{3}$, a right-handed state with frequency $\omega_+ = \omega_0 + \kappa$ and state vector

$\mathbf{a}_+ = (1\ e^{i2\pi/3}\ e^{i4\pi/3})^{\mathrm{T}}/\sqrt{3}$, and a left-handed state with the same resonance frequency $\omega_- = \omega_+ = \omega_0 + \kappa$, and state vector $\mathbf{a}_- = (1\ e^{-i2\pi/3}\ e^{-i4\pi/3})^{\mathrm{T}}/\sqrt{3}$. The transformation from the eigenbasis of the separate resonators to the eigenbasis of the static loop reads $\bar{\mathbf{a}} = \mathbf{U}^{-1}\mathbf{a}$, where $\bar{\mathbf{a}}$ is the state vector in the eigenbasis of the static loop and $\mathbf{U} = (\mathbf{a}_{\mathrm{c}}\ \mathbf{a}_+\ \mathbf{a}_-)$. Equation (1) then becomes

$$\begin{aligned}\dot{\bar{\mathbf{a}}} &= (-i\bar{\mathbf{\Omega}} - \bar{\mathbf{\Gamma}})\bar{\mathbf{a}} + \bar{\mathbf{D}}^{\mathrm{T}}\mathbf{s}^{\mathrm{inc}} \\ \mathbf{s}^{\mathrm{ref}} &= \bar{\mathbf{C}}\mathbf{s}^{\mathrm{inc}} + \bar{\mathbf{D}}\bar{\mathbf{a}}\end{aligned} \tag{5}$$

where

$$\begin{aligned}\bar{\mathbf{\Omega}} = \mathbf{U}^{\mathrm{H}}\mathbf{\Omega}\mathbf{U} &= \underbrace{\begin{pmatrix}\omega_{\mathrm{c}} & 0 & 0\\ 0 & \omega_+ & 0\\ 0 & 0 & \omega_-\end{pmatrix}}_{\bar{\mathbf{\Omega}}_0} \\ &\quad + \underbrace{\frac{\delta\omega_{\mathrm{m}}}{2}\begin{pmatrix}0 & e^{-i\omega_{\mathrm{m}}t} & e^{i\omega_{\mathrm{m}}t}\\ e^{i\omega_{\mathrm{m}}t} & 0 & e^{-i\omega_{\mathrm{m}}t}\\ e^{-i\omega_{\mathrm{m}}t} & e^{i\omega_{\mathrm{m}}t} & 0\end{pmatrix}}_{\delta\bar{\mathbf{\Omega}}_{\mathrm{m}}}\end{aligned} \tag{6}$$

$$\bar{\mathbf{\Gamma}} = \mathbf{U}^{\mathrm{H}}\mathbf{\Gamma}\mathbf{U} = \begin{pmatrix}\gamma_{\mathrm{c}} & 0 & 0\\ 0 & \gamma_+ & 0\\ 0 & 0 & \gamma_-\end{pmatrix} \tag{7}$$

$$\bar{\mathbf{D}} = \mathbf{D}\mathbf{U} = \begin{pmatrix}d_{\mathrm{c}} & d_+ & d_-\\ d_c & d_+e^{i2\pi/3} & d_-e^{-i2\pi/3}\\ d_c & d_+e^{i4\pi/3} & d_-e^{-i4\pi/3}\end{pmatrix}. \tag{8}$$

In these equations, $\gamma_{\mathrm{c}} = \gamma + 2\zeta$ and $\gamma_+ = \gamma_- = \gamma - \zeta$ are the decay rates of the common and rotating modes, respectively, while $d_{\mathrm{c}} = d + 2g$ and $d_+ = d_- = d - g$ are the coupling coefficients between these modes and the lines. Equation $\mathbf{D}^{\mathrm{H}}\mathbf{D} = 2\mathbf{\Gamma}_{\mathrm{cpl}}$ is form-invariant under the eigenbasis transformation, yielding $d_{\mathrm{c}} = \sqrt{2\gamma_{\mathrm{c,cpl}}/3}$ and $d_+ = d_- = \sqrt{2\gamma_{+,\mathrm{cpl}}/3}$, where $\gamma_{\mathrm{c,cpl}}$, $\gamma_{+,\mathrm{cpl}}$, and $\gamma_{-,\mathrm{cpl}}$ are the parts of γ_{c}, γ_+, and γ_- referring to leakage to the external lines. In the eigenbasis of the static loop, the state vectors of the common, right-handed, and left-handed eigenstates become $\bar{\mathbf{a}}_{\mathrm{c}} = (1\ 0\ 0)^{\mathrm{T}}$, $\bar{\mathbf{a}}_+ = (0\ 1\ 0)^{\mathrm{T}}$, and $\bar{\mathbf{a}}_- = (0\ 0\ 1)^{\mathrm{T}}$, respectively.

B. Eigenstates of the Source-Free System

Before solving the source-driven problem (5), it is important to study the eigenstates of the modulated loop. For simplicity of analysis, we assume $\bar{\mathbf{\Gamma}} = 0$, i.e., no loss and no coupling to the external lines. The eigenstates of the modulated-system are perturbations of the static ones, and each of them consists of two parts: a dominant one, which is the same as in the static system, apart from a small frequency detuning, and a secondary one, which is a superposition of the static eigenstates at frequencies $\omega_{\mathrm{m}i} + n\omega_{\mathrm{m}}$, where $\omega_{\mathrm{m}i}$ is the frequency of the dominant one and n is an integer. Notice that $\omega_{\mathrm{m}i} + n\omega_{\mathrm{m}}$ are the harmonics of the modulated system. For example, consider the right-handed eigenstate of the modulated system, i.e., the eigenstate that is the perturbation of the static-system right-handed eigenstate. The dominant part of this eigenstate reads

$$\bar{\mathbf{a}}_{\mathrm{m}+}^{(1)} = \bar{\mathbf{a}}_+ e^{-i\omega_{\mathrm{m}+}t} \tag{9}$$

while the secondary part is given by

$$\begin{aligned}\bar{\mathbf{a}}_{\mathrm{m}+}^{(2)} &= \bar{\mathbf{a}}_+ \sum_{\substack{n=-\infty\\ n\neq 0}}^{\infty} A_{+,n}e^{-i(\omega_{\mathrm{m}+}+n\omega_{\mathrm{m}})t} \\ &\quad + \bar{\mathbf{a}}_- \sum_{n=-\infty}^{\infty} A_{-,n}e^{-i(\omega_{\mathrm{m}+}+n\omega_{\mathrm{m}})t} \\ &\quad + \bar{\mathbf{a}}_{\mathrm{c}} \sum_{n=-\infty}^{\infty} A_{\mathrm{c},n}e^{-i(\omega_{\mathrm{m}+}+n\omega_{\mathrm{m}})t}\end{aligned} \tag{10}$$

where $A_{\mathrm{c},n}$, $A_{+,n}$, and $A_{-,n}$ are the complex amplitudes of the modulated-system harmonics. Substituting (9) and (10) into (5) results in an ordinary eigenvalue problem, the solution of which determines $\omega_{\mathrm{m}+}$ and the coefficients in (10). Keeping only terms up to first order with respect to $\delta\omega_{\mathrm{m}}$, it can be shown (see Appendix A for details) that

$$\begin{aligned}\omega_{\mathrm{m}+} &= \omega_+ - \frac{\Delta\omega}{2} \\ \bar{\mathbf{a}}_{\mathrm{m}+} &= \bar{\mathbf{a}}_+ e^{-i\omega_{\mathrm{m}+}t} - \frac{\Delta\omega}{\delta\omega_{\mathrm{m}}}\bar{\mathbf{a}}_- e^{-i(\omega_{\mathrm{m}+}-\omega_{\mathrm{m}})t} \\ &\quad + \frac{\delta\omega_{\mathrm{m}}}{2(\omega_{\mathrm{c}} - \omega_{\mathrm{m}+} - \omega_{\mathrm{m}})}\bar{\mathbf{a}}_{\mathrm{c}} e^{-i(\omega_{\mathrm{m}+}+\omega_{\mathrm{m}})t} \\ &\quad - \frac{\Delta\omega}{2(\omega_{\mathrm{c}} - \omega_{\mathrm{m}+} + 2\omega_{\mathrm{m}})}\bar{\mathbf{a}}_{\mathrm{c}} e^{-i(\omega_{\mathrm{m}+}-2\omega_{\mathrm{m}})t}.\end{aligned} \tag{11}$$

If the eigenfrequencies of the common and rotating states are far from each other, so that $\delta\omega_{\mathrm{m}}, \omega_{\mathrm{m}} \ll |\omega_+ - \omega_{\mathrm{c}}|$, the common-mode terms in (11) can be neglected and $\bar{\mathbf{a}}_{\mathrm{m}+}$ becomes

$$\bar{\mathbf{a}}_{\mathrm{m}+} = \bar{\mathbf{a}}_+ e^{-i\omega_{\mathrm{m}+}t} - \frac{\Delta\omega}{\delta\omega_{\mathrm{m}}}\bar{\mathbf{a}}_- e^{-i(\omega_{\mathrm{m}+}-\omega_{\mathrm{m}})t}. \tag{12}$$

The condition $\delta\omega_{\mathrm{m}}, \omega_{\mathrm{m}} \ll |\omega_+ - \omega_{\mathrm{c}}|$ implies negligible coupling between common and rotating modes: coupling between eigenstates with different eigenfrequencies, such as the common and rotating states, is strong either if the modulation frequency is close to the difference of the eigenfrequencies or if the modulation amplitude is very large. This is consistent with the fact that (12) can also be derived by neglecting the first row and column of $\delta\bar{\mathbf{\Omega}}_{\mathrm{m}}$ in (5), which describe the coupling between common and rotating states. The condition $\delta\omega_{\mathrm{m}}, \omega_{\mathrm{m}} \ll |\omega_+ - \omega_{\mathrm{c}}|$ also ensures operation far from the parametric-oscillation conditions $\omega_{\mathrm{m}} \approx 2\omega_+$ and $\omega_{\mathrm{m}} \approx \omega_{\mathrm{c}} + \omega_+$, where instabilities are expected and CMT breaks down. The eigenfrequency $\omega_{\mathrm{m}-}$ and state vector $\bar{\mathbf{a}}_{\mathrm{m}-}$ of the modulated-system left-handed eigenstate can be found through a similar analysis as

$$\begin{aligned}\omega_{\mathrm{m}-} &= \omega_- + \frac{\Delta\omega}{2} \\ \bar{\mathbf{a}}_{\mathrm{m}-} &= \bar{\mathbf{a}}_- e^{-i\omega_{\mathrm{m}-}t} + \frac{\Delta\omega}{\delta\omega_{\mathrm{m}}}\bar{\mathbf{a}}_+ e^{-i(\omega_{\mathrm{m}-}+\omega_{\mathrm{m}})t}.\end{aligned} \tag{13}$$

Fig. 3 shows a frequency diagram of the modulated-system right- and left-handed eigenstates. Observe that these states are separated from each other by $\Delta\omega$, an effect that resembles frequency-splitting of counter-polarized waves in magnetized ferrites, thereby providing a direct evidence for the nonreciprocal properties of the modulated system.

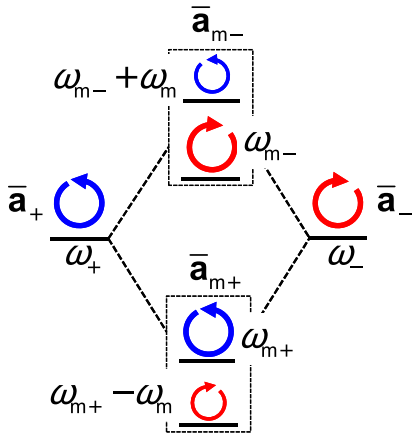

Fig. 3. Frequency diagram for the spatiotemporally modulated loop of coupled resonators. Without modulation, the loop supports degenerate counter-rotating states $\bar{\mathbf{a}}_{\pm}$ (left- and right-hand sides). Modulation mixes these states, producing the hybrid states $\bar{\mathbf{a}}_{\mathrm{m}\pm}$ (center), which consist of the rotating states at frequency levels separated by ω_{m}. Each of the hybrid states is dominated by one of the rotating states, making the hybrid states quasi-rotating. The quasi-rotating states exist at different frequency levels ($\omega_{\mathrm{m}\pm}$), which is a direct evidence that the modulated loop is nonreciprocal.

C. S-Parameters and Optimal Isolation Conditions for the Source-Driven System

Neglecting the common mode, which for $\delta\omega_{\mathrm{m}}, \omega_{\mathrm{m}} \ll |\omega_{+} - \omega_{\mathrm{c}}|$ is minimally affected by the modulation, we rewrite (5), including the source and decay terms, as

$$\begin{aligned}\dot{a}_{+} &= (-i\omega_{+} - \gamma_{+})a_{+} - i\frac{\delta\omega_{\mathrm{m}}}{2}e^{-i\omega_{\mathrm{m}}t}a_{-} + \mathbf{k}_{+}\mathbf{s}^{\mathrm{inc}} \\ \dot{a}_{-} &= (-i\omega_{-} - \gamma_{-})a_{-} - i\frac{\delta\omega_{\mathrm{m}}}{2}e^{i\omega_{\mathrm{m}}t}a_{+} + \mathbf{k}_{-}\mathbf{s}^{\mathrm{inc}}\end{aligned} \tag{14}$$

where a_{+} and a_{-} are the complex amplitudes of the right- and left-handed states of the loop, $\mathbf{k}_{+} = d_{+}(1\ e^{-i2\pi/3}\ e^{-i4\pi/3})$ and $\mathbf{k}_{-} = d_{-}(1\ e^{i2\pi/3}\ e^{i4\pi/3})$. Equation (14) can be solved by assuming

$$\begin{aligned}a_{+} &= a_{+}^{(0)}e^{-i\omega t} + a_{+}^{(+1)}e^{-i(\omega+\omega_{\mathrm{m}})t} \\ a_{-} &= a_{-}^{(-1)}e^{-i(\omega-\omega_{\mathrm{m}})t} + a_{-}^{(0)}e^{-i\omega t}\end{aligned} \tag{15}$$

where ω is the frequency of the incoming signal, $a_{\pm}^{(0)}$ are the amplitudes of the dominant sub-states, and $a_{\pm}^{(\pm1)}$ are the amplitudes of the secondary ones. For excitation from port 1, these amplitudes are found by substituting (15) into (14) as

$$\begin{aligned}a_{\pm}^{(0)} &= d_{+} \\ &\quad\times\frac{-i(\omega-\omega_{+}\mp\omega_{\mathrm{m}})+\gamma_{+}}{[-i(\omega-\omega_{+})+\gamma_{+}]\,[-i(\omega-\omega_{+}\mp\omega_{\mathrm{m}})+\gamma_{+}]+\delta\omega_{\mathrm{m}}^{2}/4} \\ a_{\pm}^{(\pm1)} &= d_{+} \\ &\quad\times\frac{-i\delta\omega_{\mathrm{m}}/2}{[-i(\omega-\omega_{+})+\gamma_{+}]\,[-i(\omega-\omega_{+}\mp\omega_{\mathrm{m}})+\gamma_{+}]+\delta\omega_{\mathrm{m}}^{2}/4}.\end{aligned} \tag{16}$$

Transmission to ports 2 and 3 can be calculated by substituting (15) into the second equation of (5) as

$$\begin{aligned}S_{11}(\omega) &= -1 + d_{+}\left[a_{+}^{(0)} + a_{-}^{(0)}\right] \\ S_{21}(\omega) &= d_{+}\left[a_{+}^{(0)}e^{i2\pi/3} + a_{-}^{(0)}e^{-i2\pi/3}\right] \\ S_{31}(\omega) &= d_{+}\left[a_{+}^{(0)}e^{i4\pi/3} + a_{-}^{(0)}e^{-i4\pi/3}\right].\end{aligned} \tag{17}$$

Due to the rotational symmetry of the structure, the rest of the S-parameters can be directly calculated from (17) by rotating the port indices as $(1,2,3) \rightarrow (3,1,2) \rightarrow (2,3,1)$. For example, S_{13} and S_{23} can be calculated from (17) as $S_{13} = S_{21}$ and $S_{23} = S_{31}$. Note that, apart from signals at the input frequency [S-parameters given in (17)], there are also signals at frequencies $\omega \pm \omega_{\mathrm{m}}$. For excitation from port 1, the S-parameters for these signals can be found by substituting (15) into the second of (5),

$$\begin{aligned}S_{11}(\omega-\omega_{\mathrm{m}}) = S_{21}(\omega-\omega_{\mathrm{m}}) = S_{31}(\omega-\omega_{\mathrm{m}}) = d_{+}a_{-}^{(-1)} \\ S_{11}(\omega+\omega_{\mathrm{m}}) = S_{21}(\omega+\omega_{\mathrm{m}}) = S_{31}(\omega+\omega_{\mathrm{m}}) = d_{+}a_{+}^{(+1)}.\end{aligned} \tag{18}$$

The rest of the S-parameters at $\omega \pm \omega_{\mathrm{m}}$ can be found again via rotation of the port indices.

Due to its threefold symmetry, the modulated loop operates as a circulator, if the signal at one of the output ports is equal to zero. For the modulation phase used here (0°, 120°, and 240° for resonators 1–3, respectively), this condition is satisfied at port 3, if the frequency of the incident wave is ω_{+} and

$$\delta\omega_{\mathrm{m}} = 2\sqrt{\frac{\gamma_{+}\left(\omega_{\mathrm{m}}^{2}+\gamma_{+}^{2}\right)}{\omega_{\mathrm{m}}\sqrt{3}-\gamma_{+}}}. \tag{19}$$

Observe that, in order for $\delta\omega_{\mathrm{m}}$ to be real, the modulation frequency should be larger than $\gamma_{+}/\sqrt{3}$. When (19) is satisfied, it is easy to show from (16) that the right- and left-handed states are, respectively, excited with phases $\pi/6$ and $-\pi/6$ at port 1. Their phases become $\pi/6+4\pi/3 = 3\pi/2$ and $-\pi/6-4\pi/3 = -3\pi/2$ at port 3, leading to mutual cancellation by destructive interference at this port. Since no power is transferred to port 3, one may think that, in the absence of loss, transmission to port 2 is ideal. However, this is not correct since, as already hinted, the modulation results in allocating part of the energy to frequencies outside the main band in the form of intermodulation products. Under the ideal modulation condition (19), it can be found from (16) and (17) that the transmission at the output port (port 2) and reflection at the input port (port 1) are, respectively, given by

$$|S_{21}(\omega_{+})| = \gamma_{+,\mathrm{cpl}}\left(\frac{1}{\gamma_{+}} - \frac{1}{\omega_{\mathrm{m}}\sqrt{3}}\right) \tag{20}$$

$$|S_{11}(\omega_{+})| = 1 - |S_{21}(\omega_{+})|. \tag{21}$$

Observe that, since $\gamma_{+,\mathrm{cpl}} < \gamma_{+}$, $|S_{21}(\omega)| < 1$, as expected from the conversion of part of the power to intermodulation

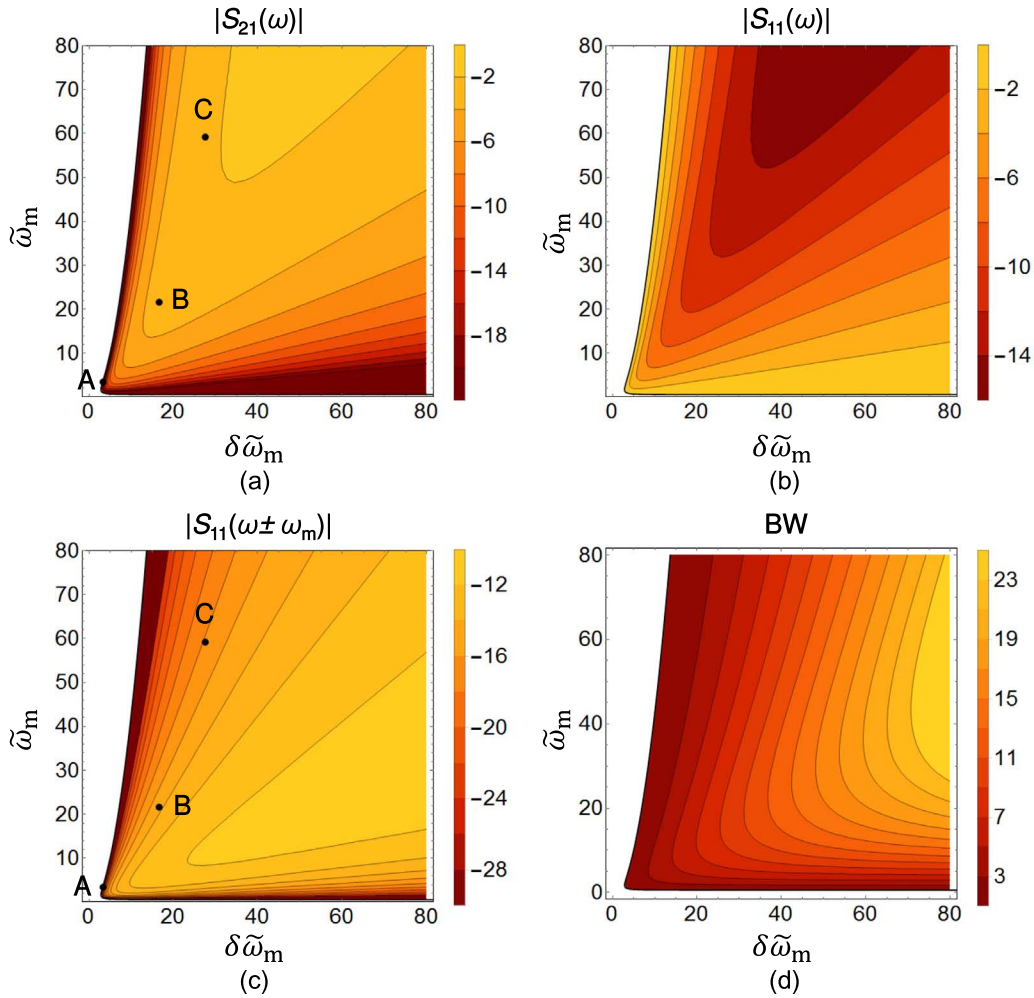

Fig. 4. Design charts for magnetic-free circulators based on loops of modulated resonators. (a) Insertion loss, $|S_{21}(\omega_+)|$, (b) return loss, $|S_{11}(\omega_+)|$, (c) intermodulation products, $|S_{21}(\omega_+ \pm \omega_m)|$, and (d) BW versus the normalized modulation frequency, $\tilde{\omega}_m = \omega_m/\gamma_{+,loss}$, and the normalized modulation amplitude, $\delta\tilde{\omega}_m = \delta\omega_m/\gamma_{+,loss}$. All the results were derived under condition (19) to obtain maximum isolation. Point A corresponds to the design in [38], point B to the lumped-element design in Section III, and point C to the distributed-element design in Section III. Inside the white regions, infinite isolation is impossible.

products. The intermodulation products at any port are found from (16) and (18) as

$$|S_{21}(\omega_+ \pm \omega_m)| = \sqrt{\frac{1}{3}|S_{21}(\omega_+)|\left[\frac{\gamma_{+,cpl}}{\gamma_+} - |S_{21}(\omega_+)|\right]}. \quad (22)$$

The transmission bandwidth (BW), another important parameter of the structure, is given by $2\gamma_+$ and it satisfies

$$BW = 2\gamma_+ = \sqrt{3}\omega_m\left[1 - \frac{\gamma_+}{\gamma_{+,cpl}}|S_{21}(\omega_+)|\right]. \quad (23)$$

Considering that $\gamma_{+,cpl} \le \gamma_+$, where the equality holds in the absence of loss, (22) and (23) lead to the following expressions, involving only $|S_{21}(\omega_+)|$:

$$|S_{21}(\omega_+ \pm \omega_m)| \le \sqrt{\frac{1}{3}|S_{21}(\omega_+)|\left[1 - |S_{21}(\omega_+)|\right]} \quad (24)$$

$$BW \le \sqrt{3}\omega_m\left[1 - |S_{21}(\omega_+)|\right]. \quad (25)$$

Equation (24) shows that the intermodulation products tend to zero, as the transmission approaches unity, as expected from power conservation. On the other hand, (25) reveals a fundamental tradeoff between BW and transmission. For a specified modulation frequency, BW decreases, as transmission increases. In order to increase transmission without affecting the BW, it is necessary to increase the modulation frequency.

Fig. 4 presents $|S_{21}(\omega_+)|$, $|S_{21}(\omega_+ \pm \omega_m)|$, $|S_{11}(\omega_+)|$ and BW versus $\delta\tilde{\omega}_m = \delta\omega_m/\gamma_{+,loss}$ and $\tilde{\omega}_m = \omega_m/\gamma_{+,loss}$ under the infinite-isolation condition (19). In these plots we use the normalized modulation parameters, $\delta\tilde{\omega}_m$ and $\tilde{\omega}_m$, instead of the absolute ones, $\delta\omega_m$ and ω_m, in order to keep the plots valid for any $\gamma_{+,loss}$, which is generally a structure-dependent parameter over which we have little control. By using the normalized parameters $\delta\tilde{\omega}_m$ and $\tilde{\omega}_m$ we essentially consider $\gamma_{+,loss}$ as a reference for all frequency quantities. It should be noted that $2\gamma_{+,loss}$ is the BW of the intrinsic resonance of the system, i.e., the resonance under negligible coupling to the external lines, and, as such, it also represents a lower bound for the BW of the loaded system. Considering that the intrinsic Q-factor of the system is given by $Q_{+,loss} = \omega_+/(2\gamma_{+,loss})$, the normalized modulation parameters in Fig. 4 can also be expressed as $\delta\tilde{\omega}_m = 2Q_{+,loss}\delta\omega_m/\omega_+$ and $\tilde{\omega}_m = 2Q_{+,loss}\omega_m/\omega_+$. The

white region in Fig. 4 corresponds to values of the modulation parameters for which infinite isolation is impossible. Furthermore, the charts in Fig. 4 are valid, provided that the conditions $\omega_{\rm m}, \delta\omega_{\rm m} \ll |\omega_+ - \omega_{\rm c}|$, under which (14) have been derived, hold. Assuming that $\omega_{\rm c} \ll \omega_+$, as it happens for the structures presented in Section III, these conditions become $\omega_{\rm m}, \delta\omega_{\rm m} \ll \omega_+$. In terms of normalized parameters, these conditions can be written as $\delta\tilde{\omega}_{\rm m}, \tilde{\omega}_{\rm m} \ll 2Q_{+,\rm loss}$, showing that the plots in Fig. 4 are valid for a particular range of values for $\delta\tilde{\omega}_{\rm m}$ and $\tilde{\omega}_{\rm m}$. Through numerical calculations, we have found that $0.1Q_{+,\rm loss}$ and $0.5Q_{+,\rm loss}$ are good upper bounds for $\tilde{\omega}_{\rm m}$ and $\delta\tilde{\omega}_{\rm m}$, respectively. Fig. 4 allows designing structures with a specified response, in terms of $|S_{21}(\omega_+)|$, $|S_{21}(\omega_+ \pm \omega_{\rm m})|$, $|S_{11}(\omega_+)|$ and BW, for given $\gamma_{+,\rm loss}$ or $Q_{+,\rm loss}$.

The charts in Fig. 4 allow reaching interesting conclusions about the effect of the modulation parameters on the characteristics of the structure. First of all, insertion and return losses generally decrease when both $\tilde{\omega}_{\rm m}$ and $\delta\tilde{\omega}_{\rm m}$ increase. On the other hand, intermodulation products tend to decrease as $\tilde{\omega}_{\rm m}$ increases. This behavior is consistent with (13), where the term $\Delta\omega/\delta\omega_{\rm m}$, providing the amplitude of the undesired secondary sub-states of the modulated loop decreases as $\omega_{\rm m}$ increases. Apart from leading to smaller reflection, larger transmission and smaller intermodulation products, increasing $\omega_{\rm m}$ is also advantageous from an implementation point of view: a large $\omega_{\rm m}$, and therefore a large separation between the wanted frequency response and the unwanted intermodulation products, results in less steep filters for the rejection of these products, and therefore easier fabrication. The charts in Fig. 4 and the above general conclusions will be used in the next section in order to design two magnetic-free microwave circulators based on lumped and distributed elements for low- and high-frequency applications, respectively.

III. Circulator Designs

A. Lumped-Element Design

The concept of angular-momentum-induced nonreciprocity was experimentally demonstrated in [38] through a ring of capacitively modulated LC resonators, as in Fig. 5(a). The most straightforward way to realize a modulated capacitor is through a varactor and a diplexer, as in Fig. 5(b). If the transmission phase between the high-frequency and common ports of the diplexer is zero, the input impedance at the high-frequency port is equal to the impedance of the modulated varactor. Furthermore, the diplexer makes sure that the modulation and input signals do not mix with each other outside the varactor. Although functional, the circuit in Fig. 5(b) has a major drawback: the diplexer is part of the resonant network—the input signal needs to go through the diplexer in order to reach the varactor—potentially complicating the design and detrimentally affecting the overall performance. For this reason, [38] followed an alternative approach to move the diplexers outside the resonant circuit. By combining the circuit in Fig. 5(a) with a dual one consisting of shunt inductors and series capacitors, the ring in [38] was designed to resonate at both the input and modulation frequencies, thus eliminating the need of separate modulation lines and diplexers. Such an approach led to very large isolation

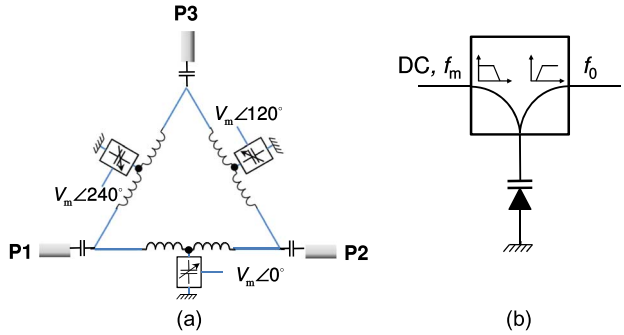

Fig. 5. Circulator based on a ring resonator, as in [38]. (a) Ring of capacitively modulated LC resonators. (b) Implementation of a variable capacitor through a varactor and a diplexer.

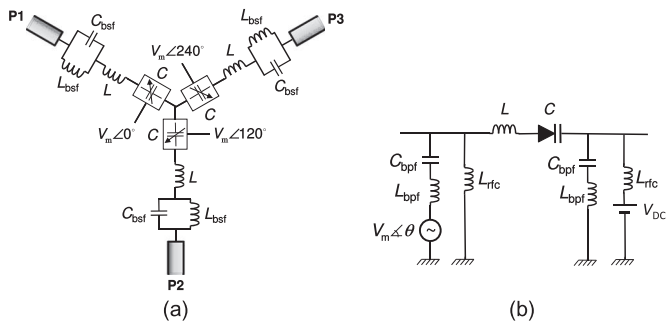

Fig. 6. Circulator based on a wye resonator. (a) Capacitively modulated lumped-element wye resonator. The parallel LC bandstop filters ($L_{\rm bsf}$ and $C_{\rm bsf}$) are used to prevent the modulation signal from leaking to the external lines. (b) Implementation of the variable capacitors through varactors and filters that create a low-impedance path for bias and modulation signals, while they block the input signal.

(more than 50 dB), but also quite large insertion loss (22 dB). The reason is that, in order to avoid interference between the main and modulation sub-circuits of the ring, the modulation frequency had to be selected quite far from the input frequency, forcing the circulator to operate in the sub-optimal bottom-left area in Fig. 4. Indeed, from the data provided in [38], it can be found that the corresponding circuit operates at point A in Fig. 4.

The aforementioned problems related to the ring topology may be overcome using the wye topology in Fig. 6(a) [40]. Modulation can be achieved by connecting varactors between filters, as in Fig. 6(b), which provide a low-impedance path for the dc and modulation signals, while they exhibit very large impedance for the input signal. A simple implementation of such a filter involves a parallel combination of a choke inductor ($L_{\rm rfc}$), which provides a low-impedance path for the dc signal, and a series LC bandpass filter ($L_{\rm bpf}$ and $C_{\rm bpf}$), which, if designed to resonate at the modulation frequency, provides a low-impedance path for the modulation signal. Furthermore, the filter is designed to have large impedance at the resonance frequency of the circuit, in order to block the input signal. For the filters connecting the circuit ports and the inductors L, such as the filter on the left-hand side of the varactor in Fig. 6(b), this condition is satisfied if $Z_{\rm filter}(\omega_0) \gg Z_0$, where $Z_{\rm filter}(\omega_0)$ is the filter impedance at the circuit resonance frequency ω_0, considering that, at ω_0, the impedance at the position of the filters looking towards the ports and the varactors is Z_0 and $Z_0/2$, respectively.

Through a similar analysis, it is possible to show that the condition $Z_{\rm filter}(\omega_0) \gg Z_0$ is also sufficient to minimize the flow of the input signal through the filter connected at the center node of the circuit [filter at the right-hand side of the varactor in Fig. 6(b)]. Filters can also be connected between the external lines and the inductors of the wye circuit in order to prevent the modulation signals from leaking to the external lines. These filters can be simple parallel LC bandstop filters ($L_{\rm bsf}$ and $C_{\rm bsf}$), which, although exhibiting a narrow BW, they can effectively block the monochromatic modulation signal. Interestingly, none of the filters in the wye-circuit design intercepts the path of the input signal inside the resonant circuit formed by the varactors and the inductors L, and as a result their effect on the operation of the device at the input frequency is expected to be minimal.

The resonant states of the wye resonator can be calculated by terminating the transmission lines with matched loads, and assuming no external excitation. Conservation of charge at the center node of the circuit demands that the total charge of the three capacitors is zero. This fact excludes the presence of a common state, which would require all the capacitors to have the same charge and, as a result, the total charge to be nonzero. On the other hand, charge conservation is satisfied by the rotating states since for such states the total charge is by definition zero, as a result of their threefold symmetry, with 120° phase difference between different resonators. The threefold symmetry of the rotating states also requires that the voltage at the center node of the circuit is zero. Considering that at resonance the current flow is nonzero, the total impedance of each branch is then zero, yielding

$$\omega_\pm = \sqrt{\frac{1}{LC} - \frac{Z_0^2}{4L}}$$
$$\gamma_\pm = \frac{Z_0}{2L} \tag{26}$$

where Z_0 is the characteristic impedance of the transmission lines. For $\gamma_\pm \ll \omega_\pm$, i.e., for a circuit with a large Q-factor, $\omega_\pm \approx 1/\sqrt{LC}$. A capacitance perturbation $\delta C_{\rm m}$ then produces a frequency perturbation $\delta\omega_{\rm m} = \omega_\pm \delta C_{\rm m}/(2C)$. Loss in the inductors and varactors can be represented by a series resistance R, and in such a case, Z_0 in (26) should be replaced by $Z_0 + R$. It is obvious that $Z_0/(2L)$ and $R/(2L)$ correspond to the leakage and loss decay rates, $\gamma_{\pm,\rm cpl}$ and $\gamma_{\pm,\rm loss}$, respectively. The corresponding Q-factors then read $Q_{\rm cpl} = \sqrt{L/C}/Z_0 = \omega_\pm L/Z_0$ and $Q_{\rm loss} = \sqrt{L/C}/R = \omega_\pm L/R$. The fact that the wye resonator does not have a common state indicates that the coupled-mode analysis in Section II is only restricted by the parametric oscillation condition $\omega_{\rm m} \approx 2\omega_\pm$. A full circuit analysis for the wye resonator, including modulation and excitation from the external lines, is presented in Appendix B.

Based on the above analysis, we designed a circulator for operation at 200 MHz ($\omega_\pm = 200$ MHz), with a target resonance BW of 10% ($Q = 10$). Considering that R can be much smaller than Z_0 for good-quality inductors, we find that the values of L and C that satisfy these specifications are 400 nH and 1.6 pF, respectively. Based on these values and commercially available components, we choose the lumped elements listed in Table I. Furthermore, the modulation frequency is chosen as 40 MHz, resulting in operation at point B in Fig. 4, where the insertion loss and intermodulation products are 3.1 and −16 dB, respectively. Note that at 200 MHz the inductors $L_{\rm bpf}$ and $L_{\rm rfc}$ operate above self-resonance, and as a result, their effective response at this frequency is capacitive and very lossy. However, since their impedance is very large, they can still efficiently prevent the input signal from leaking to the modulation lines. This fact shows that for the wye topology, contrary to the ring topology, it is not necessary for the filter components to operate optimally at both the modulation and input frequencies, thereby significantly relaxing the design constraints. Note that, for simplicity purposes, in the proof-of-concept design presented here, the bandstop filters used to prevent the modulation signals from leaking to the external lines [filters $L_{\rm bsf} - C_{\rm bsf}$ in Fig. 6(a)] are omitted. The effect of these filters on the input signal is minimal since the capacitors $C_{\rm bsf}$, through which the input signal primarily flows, have a self-resonance frequency much larger than the operation frequency.

TABLE I
LUMPED ELEMENT VALUES FOR THE CIRCUIT IN FIG. 6

Component	Value	Equivalent Series Resistance	Self-Resonance Frequency
L	560 nH	~ 12 Ω at 200 MHz (Q-factor of 55)	600 MHz
C	Skyworks SMV1233 $V_{\rm dc}$ ~ 4.5 V	1.2 Ω	–
$L_{\rm bpf}$	Coilcraft 1.5 μH	–	190 MHz
$C_{\rm bpf}$	American Technical Ceramics 11 pF	~ 0.05 Ω	~ 4 GHz
$L_{\rm rfc}$	Coilcraft 1.5 μH	–	190 MHz

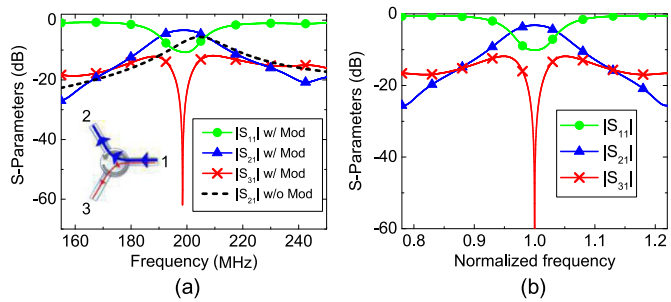

Fig. 7. Scattering parameters for the lumped-element wye resonator without modulation and under the optimum modulation condition. (a) Full-wave simulations. (b) Coupled-mode analysis.

Fig. 7 presents the S-paramaters with and without modulation as obtained through full-wave simulations and the coupled-mode (17). Simulations were performed by considering full SPICE models for the varactors and the filter inductors, while inductors L were modeled through a series combination of inductances and resistances, as listed in Table I, considering that these inductors operate well below their self-resonances. Without modulation, the input power is equally split to the output ports. When modulation is applied, the signal is transmitted to port 3 with insertion loss of about 3.4 dB, a little larger than at point B in Fig. 4, due to additional

loss introduced by the filters, while the power transmitted to port 2 is negligible (isolation is larger than 50 dB), showing a remarkable improvement in the performance compared to the ring topology. The numerical results are in excellent agreement with the theoretical ones, apart from a slight shift in the resonance frequency in simulations when the modulation is applied. As shown in Appendix B, this is a second-order effect with respect to $\delta C_{\rm m}$ that cannot be captured by first-order CMT.

Fig. 7 shows that the circuit exhibits a return loss of -10 dB, which, although not ideal, can be considered acceptable for practical applications. An interesting question that now arises is whether the return loss may be reduced by impedance matching. Matching the proposed circulator is equivalent to matching a lossy device, considering that intermodulation conversion in the proposed circulator is by all means a loss channel at the fundamental frequency, given the overall passivity of the device. Ideal matching of a lossy three-port circulator is possible only if the common mode of the circulator can absorb power [42]. This can be proven by considering that the S-matrix of a lossy circulator with infinite isolation reads

$$\mathbf{S} = \begin{pmatrix} S_{11} & 0 & S_{21} \\ S_{21} & S_{11} & 0 \\ 0 & S_{21} & S_{11} \end{pmatrix}. \tag{27}$$

It is then not difficult to show that the eigenvalue associated with the common mode of the system, i.e., the reflection coefficient of the common mode, is given by $S_{11} + S_{21}$ and, as a result, the power absorbed by the common mode is equal to $1 - |S_{11} + S_{21}|^2$. It is clear that zero reflection, $S_{11} = 0$, is only possible if the common mode can absorb power, as mentioned before. For the simple wye resonators considered here such an effect is impossible, because these resonators do not support a common mode at all. Nevertheless, according to (21), it is possible to achieve very small values of S_{11} if the modulation parameters are appropriately selected so that S_{21} is close to unity. Total reflection cancellation may be possible by adding networks between the ports and the branches of the circulator that allow the excitation of a common mode. However, this is not a trivial problem and falls beyond the scope of this work.

Intermodulation frequencies are unavoidable by-products of the proposed concept and, therefore, it is important to know how strong they are. Fig. 8 plots the S-parameters at the center frequency f_0 and the inter-modulation frequencies $f_0 \pm nf_{\rm m}$, for the modulation parameters in Fig. 7. Both in simulations and theory, the first-order intermodulation products $f_0 \pm f_{\rm m}$ are about 14 dB lower than the output power, a bit higher than at point B in Fig. 4(c), due to additional loss in the filters. Numerical simulations reveal the existence of additional higher order intermodulation products $f_0 \pm nf_{\rm m}$ with $n > 1$, which result from higher order modulation terms at frequencies $nf_{\rm m}$, due to the nonlinear response of the varactors. These products are much weaker than the first-order intermodulation products and they are completely absent for perfectly linear varactors, as shown in Appendix B.

Varactors are nonlinear elements and, as such, they are expected to affect the maximum power that can be handled by the device. Fig. 9 presents the output power and third-order intermodulation distortion versus input power for an input signal

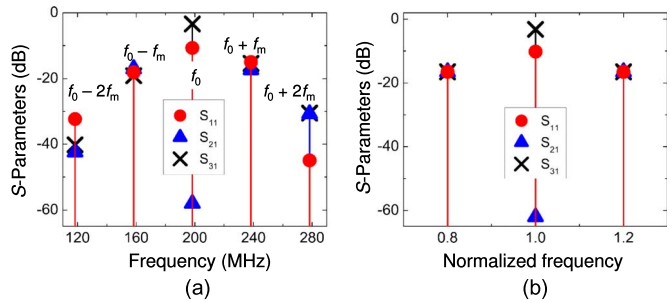

Fig. 8. S-parameters at input and intermodulation frequencies in the case of the lumped-element resonator for the modulation condition in Fig. 7. (a) Full-wave simulations. (b) Coupled-mode analysis.

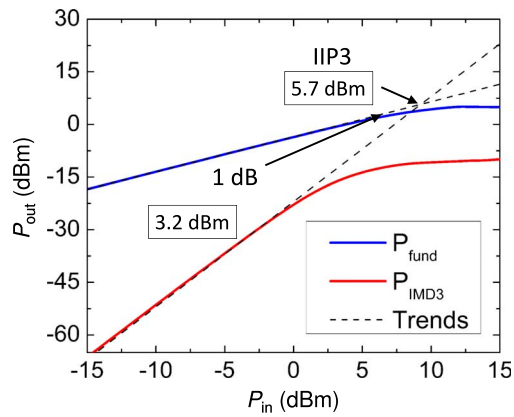

Fig. 9. Nonlinear distortion in the case of the lumped-element wye resonator of Fig. 6 for excitation with a dual-tone signal, with frequencies centered at 200 MHz and separated by 1.5 kHz. The results correspond to full-wave simulations.

consisting of two tones centered at 200 MHz, for which isolation is maximum. As in any nonlinear circuit, power saturation and intermodulation distortion are second-order nonlinear effects, related to the third power of the excitation signal or, in the case of varactors, to the coefficient C_2 in the polynomial expansion $C = C_0 + C_1 v + C_2 v^2 + \ldots$ of the varactor capacitance around the dc biasing point $V_{\rm dc}$. C_2 depends on $V_{\rm dc}$, but not on the modulation signal, showing that modulation does not affect the nonlinear properties of the structure. Ideally, we would like to completely cancel C_2, which is, however, impossible with simple varactors, like the ones used here. Nevertheless, C_2 decreases as $V_{\rm dc}$ increases, making possible to reduce nonlinear distortion by increasing $V_{\rm dc}$. In order to understand this property better, we consider a particular example of a silicon hyperabrupt varactor, like the ones used in our design, with $C - V$ relation $C_0 = C_{\rm J0}/\sqrt{1 + V/V_0}$, where $C_{\rm J0}$ is the junction capacitance and V_0 is the built-in voltage. In such a scenario, $C_2 = 3C_0/[8(V_0 + V_{\rm dc})^2]$, implying that, if $V_0 + V_{\rm dc}$ is increased by a factor of 4 and $C_{\rm J0}$ by a factor of 2 (the area of the varactor junction is increased by the same factor), so that C_0 remains the same, C_2 is reduced by a factor of 16, implying an improvement of 12 dB for the maximum power handled by the device. A drawback of this approach is that C_1, which determines the capacitance modulation, also decreases as $V_{\rm dc}$ increases, making necessary the use of a larger modulation voltage. In the previous

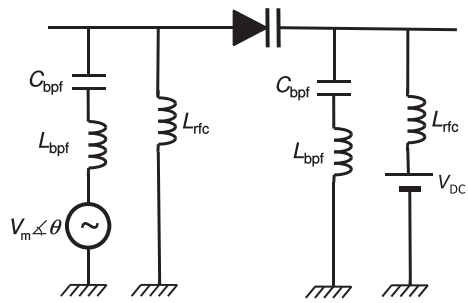

Fig. 10. Alternative implementation of the modulation network for the circuit in Fig. 6(a).

example, $C_1 = -C_0/[2(V_0 + V_{dc})]$, implying that for an increase of $V_0 + V_{dc}$ by a factor of 4 the modulation voltage is also required to increase by the same factor. This tradeoff between modulation voltage and maximum input power may be overcome through more advanced varactor topologies, such as the ones recently proposed in [43], where nonlinear distortion and capacitance modulation can be independently controlled.

The circuit in Fig. 6(a) was realized on a printed circuit board, as shown in Fig. 11(c). A photograph and a schematic of the experimental setup is shown in Fig. 11(a) and (b), respectively. The modulation signals were generated through two phase-locked RF signal generators. Modulation of the varactors was achieved through the circuit in Fig. 10, which is different from the one in Fig. 6(b) with respect to the position of the filters $L_{bpf} - C_{bpf} - L_{rfc}$. In particular, in Fig. 10, these filters are connected at the varactors' anodes, while in Fig. 6(b) they are connected between the external lines and the inductors L. At a first glance, this difference may look not important for the circulator operation. However, a closer inspection reveals that the impedance at the position of the filters towards the circuit ports in the circuit of Fig. 10 is $Z_0 + R + i\omega_0 L$, instead of Z_0, as in Fig. 6(b) and, as a result, the condition $Z_{filter}(\omega_0) \gg Z_0$ may not be sufficient. Indeed, for the lumped-element values in Table I, the modulation circuit in Fig. 10 leads to a resonance at 150 MHz, instead of 200 MHz as for the modulation circuit in Fig. 6(b). Furthermore, insertion loss with the circuit in Fig. 10 is larger than with the circuit in Fig. 6(b), due to the significant loss of L_{bpf} and L_{rfc} at the input frequency, and the fact that the input signal can now flow through these inductors. Loss can be reduced by reducing the resonance frequency since inductor loss typically decreases as frequency decreases. For the fabricated circuit, loss becomes minimum for a dc bias voltage of 1.1 V and a resonance frequency of 130 MHz.

Measured and simulated S-parameters for this geometry are presented in Fig. 12. These results provide a clear experimental demonstration of the nonreciprocal properties of the lumped-element wye circulator in Fig. 6(a) with isolation exceeding 50 dB. Furthermore, although insertion loss is larger than in Fig. 7, due to the sub-optimal connection of the filters $L_{bpf} - C_{bpf} - L_{rfc}$, as explained before, it is significantly smaller than in the preliminary design [38], which was based on the ring topology in Fig. 5(a). It is also worth noticing the good agreement between experimental and numerical results, even in terms of fine

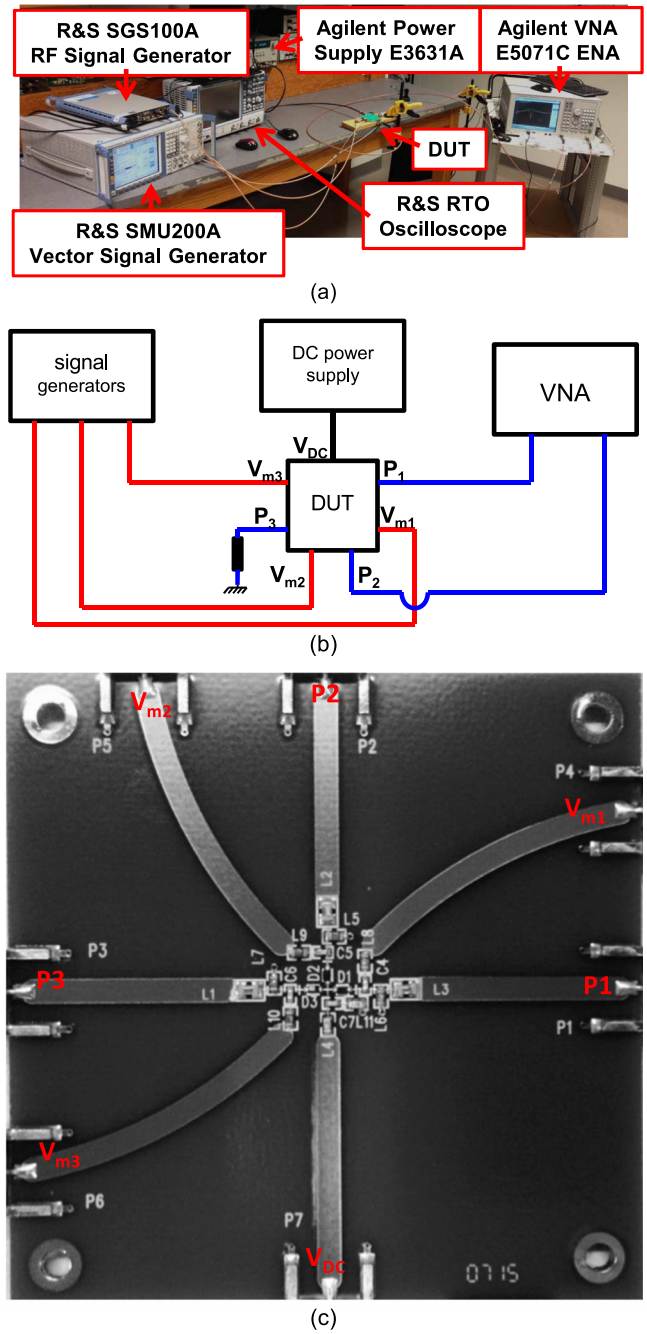

Fig. 11. Experimental demonstration of the circuit in Fig. 6(a) with the modulation network in Fig. 10. The lumped-element values are the same as in Table I. (a) Photograph of the experimental setup. The power supply provided the dc biasing of the varactors, while the signal generation the modulation signals. (b) Schematic of the experimental setup. (c) Photograph of the device-under-test (DUT).

features, such as the small bump at 140 MHz, which is related to the dispersive characteristics of L_{bpf} and L_{rfc}. This small bump disappears if L_{bpf} and L_{rfc} are modeled as a series combination of dispersionless inductances and resistances. The good agreement between experimental and numerical results is a strong indication that the numerical results in Fig. 7, corresponding to optimal connection of the filters $L_{bpf} - C_{bpf} - L_{rfc}$, are practically achievable.

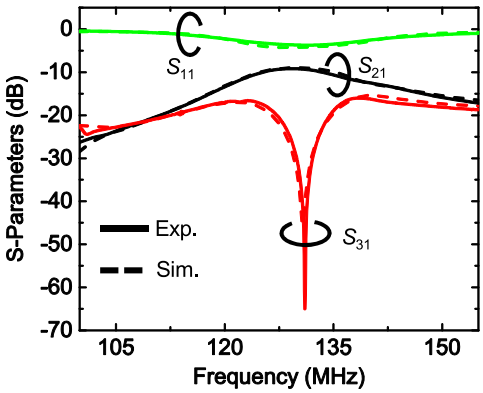

Fig. 12. Experimental and numerical results for the circuit in Fig. 6(a) with the modulation network in Fig. 10.

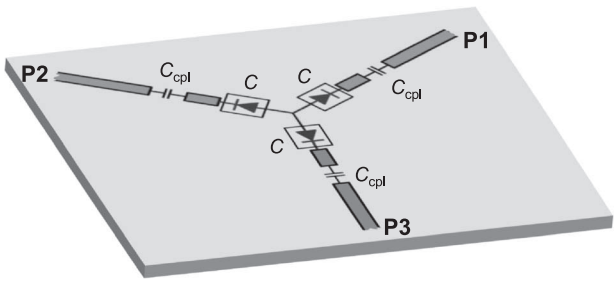

Fig. 13. Circulator based on a distributed wye resonator for high-frequency operation. The varactors and adjacent transmission line sections provide the resonance of the circuit, while the capacitors $C_{\rm cpl}$ couple the resonator to the external transmission lines.

B. Distributed-Element Design

The circulator presented in Section III-A is based on lumped elements and, as such, it is ideal for low-frequency applications. However, as the frequency increases, lumped components exhibit poorer performance, or they are totally unavailable. For this reason, in this section we present a distributed design for wireless-communications band (∼2.2 GHz), which, like the lumped-element design, is based on the wye topology, but with inductors now replaced by transmission-line sections, as in Fig. 13. The wye resonator is coupled to external lines through the capacitors $C_{\rm cpl}$. The modulation network is identical to the lumped-element case, with the only variation in the position of the bandstop filters, which are now connected between the external lines and the coupling capacitors. Since the distributed-element design does not present any significantly different fabrication challenges than the lumped-element design, and considering the excellent agreement between experimental and full-wave simulation results for the lumped-element design, here we present only full-wave simulation results for a realistic layout of the distributed element system. The parameters of this layout are provided in Table II.

Neglecting the coupling to external lines ($C_{\rm cpl} \to 0$), the input impedance of the transmission-line section from the side of the varactors reads $Z_{\rm TL} = iZ_0\cot(\beta l)$, where Z_0, β, and l are the characteristic impedance, wavenumber, and length of the transmission line segments. Similar to the lumped-element case, the input impedance of each branch as seen from the center node of the circuit should be zero at resonance, resulting in

TABLE II
GEOMETRICAL PARAMETERS AND LUMPED ELEMENT VALUES FOR THE CIRCUIT IN FIG. 10

Parameter	Value
Substrate	Rogers 4350
Substrate thickness	0.762 mm
Microstrip width	1.55 mm
Microstrip thickness	0.043 mm
Microstrip length	22 mm

Element	Value	Equivalent Series Resistance	Self-Resonance Frequency
C	Skyworks SMV1234 V_{dc} ~ 4 V	0.8 Ω	–
C_{cpl}	0.3 pF	0.15 Ω	20 GHz
L_{bpf}	Coilcraft 56 nH	–	2.07 GHz
C_{bpf}	2.85 pF	0.15 Ω	7 GHz
L_{rfc}	Coilcraft 56 nH	–	2.07 GHz

$$Z_0\cot(\beta l) + \frac{1}{\omega C} = 0 \tag{28}$$

which is satisfied if the length of the transmission-line sections is between a quarter-and-half wavelength. In reality, the resonance frequency is slightly lower than what predicted by (28), due to the coupling capacitors. The frequency perturbation due to a change in the varactor capacitance can be calculated from (28). In particular, by taking the derivative of (28) with respect to C it can be shown that

$$\delta\omega_0 = -\omega_0\frac{\delta C}{2C}\frac{2}{1+\beta_0 l\left[\omega_0 Z_0 C + 1/(\omega_0 Z_0 C)\right]} \tag{29}$$

where ω_0 is the resonance frequency and β_0 is the corresponding transmission-line wavenumber. Considering that $\omega_0 Z_0 C + 1/(\omega_0 Z_0 C) \geq 2$ and $\beta_0 l \geq \pi/2$, we find that $|\delta\omega_0| \leq \omega_0\delta C/(4C)$, which shows that, in the case of the distributed element design, the frequency perturbation is smaller than in the case of the lumped-element design, where $\delta\omega_0 = -\omega_0\delta C/(2C)$, by at least a factor of 2.

Based on (28), we designed a circulator for operation at 2.2 GHz. The geometrical parameters of the structure and the values of the lumped elements are provided in Table II. The structure is selected to operate at point C in Fig. 4, where insertion loss is less than 2.5 dB and intermodulation products are −20 dB. The intrinsic Q-factor of the structure, associated with the loss of the lumped elements, the substrate, and the metallic traces, was calculated as $Q_{\rm loss} = 160$, by fitting CMT to simulations in the case without modulation. In particular, substituting (16) into (17) with $\omega_{\rm m} = \delta\omega_{\rm m} = 0$ yields $S_{21} = (2/3)\gamma_{\rm cpl}/[-i(\omega-\omega_0)+\gamma]$. By fitting this expression to numerical results, we can calculate γ and $\gamma_{\rm cpl}$. Then $\gamma_{\rm loss} = \gamma - \gamma_{\rm cpl}$ and $Q_{\rm loss} = \omega_0/(2\gamma_{\rm loss})$. Note, that the value of the coupling capacitor is not important for the calculation of $Q_{\rm loss}$, because $Q_{\rm loss}$ is an inherent property of the resonator. From the

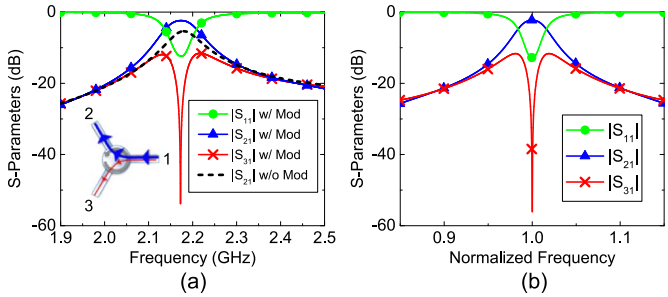

Fig. 14. Scattering parameters for the distributed wye resonator without modulation and under the optimum modulation condition. (a) Full-wave simulations. (b) Coupled-mode analysis.

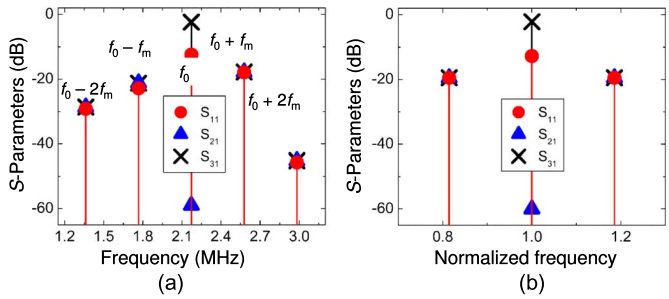

Fig. 15. S-parameters at input and intermodulation frequencies in the case of the distributed wye resonator for the modulation condition in Fig. 11. (a) Full-wave simulations. (b) Coupled-mode analysis.

value of $Q_{\rm loss}$, we found that the modulation frequency should be 400 MHz.

Fig. 14 shows the S-parameters of the structure for the optimum modulation condition. Results are similar to the lumped element case, apart from a slight asymmetry in the simulated resonance curves, resulting from a higher order resonance above 3 GHz, which does not exist in the lumped-element design. This asymmetry is not visible in the theoretical results because this higher order mode is neglected in coupled-mode analysis. Fig. 15 shows the S-parameters at the center and intermodulation frequencies for the modulation condition in Fig. 14. The intermodulation product at $f_0 - f_{\rm m}$ is 20 dB below the main signal at f_0, in perfect agreement with Fig. 4(c), while the intermodulation product at $f_0 + f_{\rm m}$ is slightly larger than $f_0 - f_{\rm m}$, due to the asymmetry created by the higher order resonance. Finally, Fig. 16 shows the nonlinear distortion for excitation by a pair of tones centered at 2.2 GHz. The maximum input power is slightly larger than in the lumped-element case.

IV. Conclusions

The concept of spatiotemporally modulated coupled resonator networks was investigated for the realization of magnetless microwave circulators. A rigorous analytical model was developed, through which the exact condition for obtaining infinite isolation was derived. The derived model, validated with numerical simulations, allows determining in closed form the required modulation parameters for given lossy Q-factor, desired insertion loss, and intermodulation products. Achieving low insertion loss generally requires large modulation parameters, while low intermodulation products can be achieved by increasing only the modulation frequency, irrespective of the

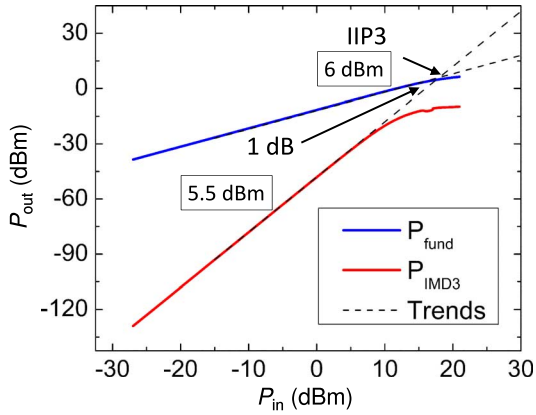

Fig. 16. Nonlinear distortion in the case of the distributed wye resonator for excitation with a dual-tone signal with frequencies centered at 2.2 GHz and separated by 15 kHz. The results correspond to full-wave simulations.

modulation amplitude. Based on the analytical model, two circulators were designed for VHF and wireless communications bands. Both designs were based on wye resonators, which were shown to be easier to realize and lead to better performance than ring resonators. Lumped and distributed elements were used for the low- and high-frequency designs, respectively. Both designs exhibit remarkable performance in terms of insertion loss and isolation, close to commercial standards for magnetic circulators.

In addition to obvious advantages in terms of cost, weight, and size reduction, an important advantage of the proposed magnetless circulators is their tunability and noise performance. Power handling is limited by the varactors through which modulation is achieved, but it can be improved by either increasing the dc bias of the varactors or using more advanced varactor configurations. The proposed designs offer a large degree of flexibility in the selection of the modulation frequency, which can be made substantially lower than the signal frequency, significantly simplifying the design of the modulation networks. However, the modulation frequency should not be very low, in order to achieve enough distance between the input and intermodulation frequencies, which is important for the efficient rejection of intermodulation products using suitable filters. The results presented in this paper constitute an important step towards the realization of integrated circulators, which may allow achieving full-duplex operation in wireless communications systems. We also point out that the proposed designs are well suited to push these concepts to very low and very high frequencies, up to ranges in which magnetic circulators are not practical, respectively, for the lumped- and distributed-element designs.

Appendix

A. Eigenstates of the Modulated Loop

Here, we calculate the eigenstates of the modulated loop in the case of zero intrinsic loss and no coupling to external lines. To this end, we need to solve (5) with $\bar{\mathbf{\Gamma}} = 0$ and $\mathbf{s}^{\rm inc} = 0$. As a first step, we solve these equations in the case of negligible coupling between the common and rotating states, which is a valid assumption if $\omega_{\rm m}, \delta\omega_{\rm m} \ll |\omega_{\rm c} - \omega_{\pm}|$. In such a case, the

first column and the first row of $\delta\bar{\mathbf{\Omega}}_{\mathrm{m}}$ can be neglected and (5) becomes

$$\begin{aligned}\dot{\tilde{a}}_{\mathrm{c}} &= -i\omega_{\mathrm{c}}\tilde{a}_{\mathrm{c}}\\ \dot{\tilde{a}}_{+} &= -i\omega_{+}\tilde{a}_{+} - \frac{i\delta\omega_{\mathrm{m}}}{2}e^{-i\omega_{\mathrm{m}}t}\tilde{a}_{-}\\ \dot{\tilde{a}}_{-} &= -i\omega_{-}\tilde{a}_{-} - i\frac{\delta\omega_{\mathrm{m}}}{2}e^{i\omega_{\mathrm{m}}t}\tilde{a}_{+}\end{aligned} \tag{30}$$

where the "tilde" is used to distinguish the approximate solution under the assumption of zero coupling between the common and rotating states from the exact one. The solution of the first of these equations is obviously $\tilde{a}_{\mathrm{c}} = A_{\mathrm{c}}e^{-i\omega_{\mathrm{c}}t}$, where A_{c} is a complex number. The solution of the other two equations can be found by assuming $\tilde{a}_{+} = A_{+}e^{-i\omega t}$ and $\tilde{a}_{-} = A_{-}e^{-i(\omega-\omega_{\mathrm{m}})t}$. Equation (30) then becomes

$$\begin{pmatrix}\omega_{+} & \dfrac{\delta\omega_{\mathrm{m}}}{2}\\ \dfrac{\delta\omega_{\mathrm{m}}}{2} & \omega_{+}+\omega_{\mathrm{m}}\end{pmatrix}\begin{pmatrix}A_{+}\\ A_{-}\end{pmatrix} = \omega\begin{pmatrix}A_{+}\\ A_{-}\end{pmatrix} \tag{31}$$

which is a typical eigenvalue problem with eigenvalues $\tilde{\omega}_{\mathrm{m}+} = \omega_{+} - \Delta\omega/2$ and $\tilde{\omega}_{\mathrm{m}}- = \omega_{+} + \Delta\omega/2 + \omega_{\mathrm{m}}$, where $\Delta\omega = \sqrt{{\omega_{\mathrm{m}}}^2 + \delta\omega_{\mathrm{m}}^2} - \omega_{\mathrm{m}}$, and corresponding eigenvectors $\mathbf{A}_{\mathrm{m}+} = (1 - \Delta\omega/\delta\omega_{\mathrm{m}})^{\mathrm{T}}$ and $\mathbf{A}_{\mathrm{m}-} = (\Delta\omega/\delta\omega_{\mathrm{m}})^{\mathrm{T}}$. The corresponding solutions of (30) read

$$\begin{aligned}\tilde{\mathbf{a}}_{\mathrm{mc}} &= \begin{pmatrix}1\\0\\0\end{pmatrix}e^{-i\omega_{\mathrm{c}}t}\\ \tilde{\mathbf{a}}_{\mathrm{m}+} &= \frac{1}{\sqrt{\Delta}}\begin{pmatrix}0\\1\\-\dfrac{\Delta\omega}{\delta\omega_{\mathrm{m}}}e^{i\omega_{\mathrm{m}}t}\end{pmatrix}e^{-i\tilde{\omega}_{\mathrm{m}+}t}\\ \tilde{\mathbf{a}}_{\mathrm{m}-} &= \frac{1}{\sqrt{\Delta}}\begin{pmatrix}0\\\dfrac{\Delta\omega}{\delta\omega_{\mathrm{m}}}e^{-i\omega_{\mathrm{m}}t}\\1\end{pmatrix}e^{-i\tilde{\omega}_{\mathrm{m}-}t}\end{aligned} \tag{32}$$

where $\Delta = 1 + (\Delta\omega/\delta\omega_{\mathrm{m}})^2$.

Next, we solve the full (5), including coupling between the common and rotating states, by transforming it to the basis defined by (32) via $\bar{\mathbf{a}} = \mathbf{V}\hat{a}$, where

$$\mathbf{V} = \frac{1}{\sqrt{\Delta}}\begin{pmatrix}\sqrt{\Delta} & 0 & 0\\ 0 & 1 & \dfrac{\Delta\omega}{\delta\omega_{\mathrm{m}}}e^{-i\omega_{\mathrm{m}}t}\\ 0 & -\dfrac{\Delta\omega}{\delta\omega_{\mathrm{m}}}e^{i\omega_{\mathrm{m}}t} & 1\end{pmatrix}. \tag{33}$$

In particular,

$$\dot{\hat{\mathbf{a}}} = -i\hat{\mathbf{\Omega}}\hat{\mathbf{a}} \tag{34}$$

where $\hat{\mathbf{\Omega}} = \mathbf{V}^{\mathrm{H}}\bar{\mathbf{\Omega}}\mathbf{V} - i\mathbf{V}^{\mathrm{H}}\dot{\mathbf{V}}$. After straightforward, but lengthy manipulations, we find

$$\begin{aligned}\hat{\mathbf{\Omega}} = \hat{\mathbf{\Omega}}_0 &+ \delta\omega_1\begin{pmatrix}0 & e^{-i\omega_{\mathrm{m}}t} & e^{i\omega_{\mathrm{m}}t}\\ e^{i\omega_{\mathrm{m}}t} & 0 & 0\\ e^{-i\omega_{\mathrm{m}}t} & 0 & 0\end{pmatrix}\\ &+\delta\omega_2\begin{pmatrix}0 & e^{i2\omega_{\mathrm{m}}t} & e^{-i2\omega_{\mathrm{m}}t}\\ e^{-i2\omega_{\mathrm{m}}t} & 0 & 0\\ e^{i2\omega_{\mathrm{m}}t} & 0 & 0\end{pmatrix}\end{aligned} \tag{35}$$

where $\hat{\mathbf{\Omega}}_0 = \mathrm{diag}\{\omega_{\mathrm{c}}, \tilde{\omega}_{\mathrm{m}+}, \tilde{\omega}_{\mathrm{m}-}\}$ and

$$\begin{aligned}\delta\omega_1 &= \frac{\delta\omega_{\mathrm{m}}}{2\sqrt{\Delta}}\\ \delta\omega_2 &= -\frac{\Delta\omega}{2\sqrt{\Delta}}.\end{aligned} \tag{36}$$

The matrix $\hat{\mathbf{\Omega}}$ is time periodic with periodicity $T_{\mathrm{m}} = 2\pi/\omega_{\mathrm{m}}$. Therefore, according to the Floquet theorem, the solution of (34) can be expressed as

$$\hat{\mathbf{a}} = \sum_{n=-\infty}^{\infty}\hat{\mathbf{a}}_{\mathrm{n}}e^{-i(\omega+n\omega_{\mathrm{m}})t} \tag{37}$$

where ω is the fundamental frequency of the mode and $\hat{a}_n$ is the state vector of the nth Floquet harmonic. Note from (37) that ω's that are different by an integer multiple of ω_{m} give the same solution and for this reason we choose $-\omega_{\mathrm{m}}/2 \le \omega - \omega_{+} \le \omega_{\mathrm{m}}/2$, which is consistent with the fact that the solution of (34) is a perturbation of the solution of (30). In the Floquet space, (34) is transformed to the regular infinite eigenvalue problem

$$\hat{\mathbf{\Omega}}_{\mathrm{F}}\hat{\mathbf{a}}_{\mathrm{F}} = \omega\hat{\mathbf{a}}_{\mathrm{F}} \tag{38}$$

where $\hat{a}_{\mathrm{F}} = (\cdots \quad \hat{a}_{-1}^{\mathrm{T}} \quad \hat{a}_{0}^{\mathrm{T}} \quad \hat{a}_{1}^{\mathrm{T}} \quad \cdots)^{\mathrm{T}}$ and $\hat{\Omega}_{\mathrm{F}}$ is the matrix whose (m,n) block relating $\hat{a}_m$ with $\hat{a}_n$ reads

$$\begin{aligned}\hat{\mathbf{\Omega}}_{\mathrm{F},mn} = (\hat{\mathbf{\Omega}}_0 - m\omega_{\mathrm{m}})\delta_{mn} + \delta\omega_1(\hat{\mathbf{\Omega}}_1\delta_{m,n+1} + \hat{\mathbf{\Omega}}_{-1}\delta_{m,n-1})\\ +\delta\omega_2(\hat{\mathbf{\Omega}}_2\delta_{m,n+2} + \hat{\mathbf{\Omega}}_{-2}\delta_{m,n-2})\end{aligned} \tag{39}$$

where

$$\hat{\mathbf{\Omega}}_1 = \hat{\mathbf{\Omega}}_{-2} = \begin{pmatrix}0&1&0\\0&0&0\\1&0&0\end{pmatrix} \quad \hat{\mathbf{\Omega}}_{-1} = \hat{\mathbf{\Omega}}_2 = \begin{pmatrix}0&0&1\\1&0&0\\0&0&0\end{pmatrix}. \tag{40}$$

A pictorial representation of $\hat{\Omega}_{\mathrm{F}}$ is provided in Fig. 17.

The matrix $\hat{\Omega}_{\mathrm{F}}$ does not have degenerate terms in the main diagonal and, as a result, conventional perturbation theory can be applied to (38) [44]. According to this theory, assuming a Hermitian matrix $\mathbf{A}^{(0)}$ with nondegenerate eigenvalues $\lambda_i^{(0)}$ and corresponding eigenvectors $\mathbf{x}_i^{(0)}$, the eigenvalues and eigenvectors of the matrix $\mathbf{A} = \mathbf{A}^{(0)} + \epsilon\mathbf{A}^{(1)}$, where $\mathbf{A}^{(1)}$ is also a Hermitian matrix and $\epsilon \ll 1$ can be calculated from

$$\begin{aligned}\lambda_i &= \lambda_i^{(0)} + \epsilon\lambda_i^{(1)} + \epsilon^2\lambda_i^{(2)} + \dots\\ \mathbf{x}_i &= \mathbf{x}_i^{(0)} + \epsilon\mathbf{x}_i^{(1)} + \dots\end{aligned} \tag{41}$$

where

$$\begin{aligned}\lambda_i^{(1)} &= \mathbf{x}_i^{(0)\mathrm{H}}\mathbf{A}^{(1)}\mathbf{x}_i^{(0)}\\ \lambda_i^{(2)} &= \sum_{j\neq i}\frac{\left|\mathbf{x}_j^{(0)\mathrm{H}}\mathbf{A}^{(1)}\mathbf{x}_i^{(0)}\right|^2}{\lambda_i^{(0)} - \lambda_j^{(0)}}\end{aligned} \tag{42}$$

and

$$\mathbf{x}_i^{(1)} = \sum_{j\neq i}\frac{\mathbf{x}_j^{(0)\mathrm{H}}\mathbf{A}^{(1)}\mathbf{x}_i^{(0)}}{\lambda_i^{(0)} - \lambda_j^{(0)}}\mathbf{x}_j^{(0)}. \tag{43}$$

Applying these formulas to $\hat{\Omega}_{\mathrm{F}}$ and keeping terms up to first order with respect to $\delta\omega_{\mathrm{m}}$, we find that the eigenfrequencies of

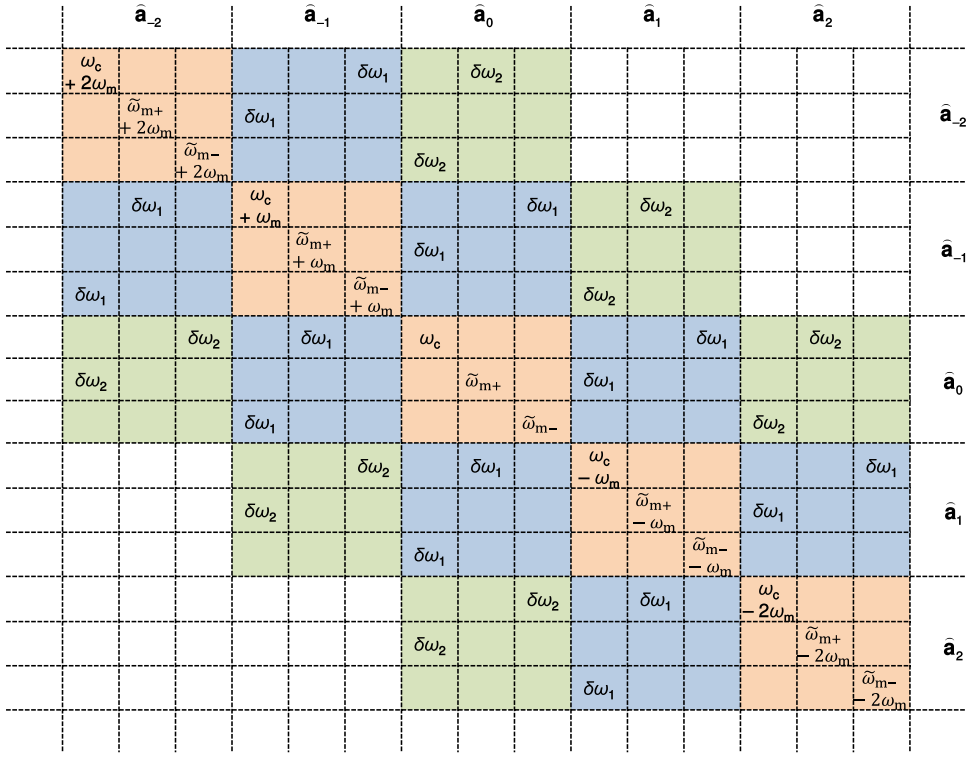

Fig. 17. Matrix $\hat{\Omega}_{\mathrm{F}}$ in (39). All the blank locations correspond to zero elements.

the common, right-handed, and left-handed states of the modulated system are the same as in the case of negligible coupling between the common and rotating states

$$\begin{aligned}\omega_{\mathrm{mc}} &= \omega_c + O\left(\delta\omega_{\mathrm{m}}^2\right)\\ \omega_{\mathrm{m}+} &= \tilde{\omega}_{\mathrm{m}+} + O\left(\delta\omega_{\mathrm{m}}^2\right)\\ \omega_{\mathrm{m}-} &= \tilde{\omega}_{\mathrm{m}-} + O\left(\delta\omega_{\mathrm{m}}^2\right).\end{aligned} \tag{44}$$

It is interesting to note that, to the first order with respect to $\delta\omega_{\mathrm{m}}$, modulation affects the frequencies of the rotating states ($\tilde{\omega}_{\mathrm{m}\pm}$ are shifted from $\omega_{\pm}$ by $\mp\Delta\omega/2$), but not the frequency of the common state. The eigenvectors of the rotating modes read

$$\begin{aligned}\bar{\mathbf{a}}_{\mathrm{m}+} =& \bar{\mathbf{a}}_{+}e^{-i\omega_{\mathrm{m}+}t} - \frac{\Delta\omega}{\delta\omega_{\mathrm{m}}}\bar{\mathbf{a}}_{-}e^{-i(\omega_{\mathrm{m}+}-\omega_{\mathrm{m}})t}\\ &+ \frac{\delta\omega_{\mathrm{m}}}{2(\omega_{\mathrm{c}} - \tilde{\omega}_{\mathrm{m}+} - \omega_{\mathrm{m}})}\bar{\mathbf{a}}_{\mathrm{c}}e^{-i(\omega_{\mathrm{m}+}+\omega_{\mathrm{m}})t}\\ &- \frac{\Delta\omega}{2(\omega_{\mathrm{c}} - \tilde{\omega}_{\mathrm{m}+} + 2\omega_{\mathrm{m}})}\bar{\mathbf{a}}_{\mathrm{c}}e^{-i(\omega_{\mathrm{m}+}-2\omega_{\mathrm{m}})t}\\ \bar{\mathbf{a}}_{\mathrm{m}-} =& \bar{\mathbf{a}}_{-}e^{-i\omega_{\mathrm{m}-}t} + \frac{\Delta\omega}{\delta\omega_{\mathrm{m}}}\bar{\mathbf{a}}_{+}e^{-i(\omega_{\mathrm{m}-}+\omega_{\mathrm{m}})t}\\ &+ \frac{\delta\omega_{\mathrm{m}}}{2(\omega_{\mathrm{c}} - \tilde{\omega}_{\mathrm{m}-} + \omega_{\mathrm{m}})}\bar{\mathbf{a}}_{\mathrm{c}}e^{-i(\omega_{\mathrm{m}+}-\omega_{\mathrm{m}})t}\\ &- \frac{\Delta\omega}{2(\omega_{\mathrm{c}} - \tilde{\omega}_{\mathrm{m}-} - 2\omega_{\mathrm{m}})}\bar{\mathbf{a}}_{\mathrm{c}}e^{-i(\omega_{\mathrm{m}-}+2\omega_{\mathrm{m}})t}.\end{aligned} \tag{45}$$

The corresponding expressions for the common mode are similar, but longer and, for this reason, they are omitted here.

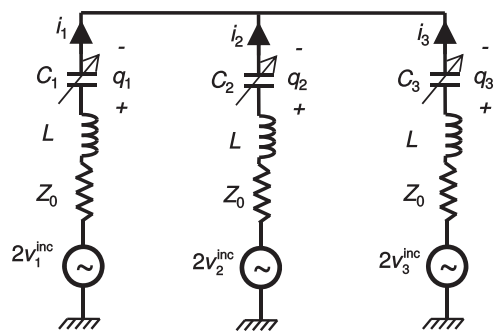

Fig. 18. Circuit schematic of the lumped-element wye resonator.

B. Full-Circuit Analysis of the Lumped-Element Circulator

Here, we provide a full-circuit analysis of the lumped-element circulator in Section III and derive exact closed-form expressions for the S-parameters of the circuit, even in the case of modulation. Furthermore, we show that modulation creates a shift in the resonance frequency of second order with respect to δC_{m}. Such an effect cannot be predicted by the first-order CMT and it requires full solution of circuit equations.

By defining the inductor currents and capacitor charges as in Fig. 18, Kirchhoff's laws read

$$i_1 + i_2 + i_3 = 0 \tag{46}$$

$$\begin{aligned}2v_1^{\mathrm{inc}} - Z_0 i_1 - L\frac{di_1}{dt} - \frac{q_1}{C_1} &= 2v_2^{\mathrm{inc}} - Z_0 i_2 - L\frac{di_2}{dt} - \frac{q_2}{C_2}\\ 2v_1^{\mathrm{inc}} - Z_0 i_1 - L\frac{di_1}{dt} - \frac{q_1}{C_1} &= 2v_3^{\mathrm{inc}} - Z_0 i_3 - L\frac{di_3}{dt} - \frac{q_3}{C_3}\\ 2v_2^{\mathrm{inc}} - Z_0 i_2 - L\frac{di_2}{dt} - \frac{q_2}{C_2} &= 2v_3^{\mathrm{inc}} - Z_0 i_3 - L\frac{di_3}{dt} - \frac{q_3}{C_3}.\end{aligned} \tag{47}$$

The sources $v_i^{\rm inc}$ stand for the incident waves from the three ports of the circuit. Summing the two first equations of (47) and replacing the term i_2+i_3 in the resulting equation with $-i_1$ from (46) yields

$$3L\frac{di_1}{dt}+3Z_0 i_1+2\frac{q_1}{C_1}-\frac{q_2}{C_2}-\frac{q_3}{C_3}=2\left(2v_1^{\rm inc}-v_2^{\rm inc}-v_3^{\rm inc}\right). \tag{48}$$

By performing the same operation to the other pairs of (47) we get

$$\begin{aligned} 3L\frac{di_2}{dt}+3Z_0 i_2-\frac{q_1}{C_1}+2\frac{q_2}{C_2}-\frac{q_3}{C_3}&=2\left(-v_1^{\rm inc}+2v_2^{\rm inc}-v_3^{\rm inc}\right)\\ 3L\frac{di_3}{dt}+3Z_0 i_3-\frac{q_1}{C_1}-\frac{q_2}{C_2}+2\frac{q_3}{C_3}&=2\left(-v_1^{\rm inc}-v_2^{\rm inc}+2v_3^{\rm inc}\right). \end{aligned} \tag{49}$$

Equation (49) can be compactly written as

$$\ddot{\mathbf{q}}+\frac{Z_0}{L}\dot{\mathbf{q}}+\frac{1}{L}\mathbf{D}\mathbf{C}^{-1}\mathbf{q}=\frac{2}{L}\mathbf{D}\mathbf{v}^{\rm inc} \tag{50}$$

where $\mathbf{q}=(q_1\ q_2\ q_3)^{\rm T}$, $\mathbf{v}^{\rm inc}=(v_1^{\rm inc}\ v_2^{\rm inc}\ v_3^{\rm inc})$, $\mathbf{C}=\mathrm{diag}\{C_1,\ C_2,\ C_3\}$, and

$$\mathbf{D}=\frac{1}{3}\begin{pmatrix}2&-1&-1\\-1&2&-1\\-1&-1&2\end{pmatrix}. \tag{51}$$

For the derivation of (50) we have also used $i_i=dq_i/dt$. In the presence of modulation, $C_n=C+\delta C_{\rm m}\cos[\omega_{\rm m}t+2(n-1)\pi/3]$ and, if $\delta C_{\rm m}\ll C$, (50) becomes

$$\ddot{\mathbf{q}}+\frac{Z_0}{L}\dot{\mathbf{q}}+\frac{1}{LC}\mathbf{D}\mathbf{q}-\frac{\delta C_{\rm m}}{LC^2}\mathbf{D}\mathbf{M}\mathbf{q}=\frac{2}{L}\mathbf{D}\mathbf{v}^{\rm inc} \tag{52}$$

where $\mathbf{M}=\mathrm{diag}\{\cos(\omega_m t),\cos(\omega_{\rm m}+2\pi/3),\cos(\omega_{\rm m}+4\pi/3)\}$.

Similarly to (1), (52) can be transformed to the eigenbasis of the common and rotating states of the ring as

$$\ddot{\tilde{\mathbf{q}}}+\frac{Z_0}{L}\dot{\tilde{\mathbf{q}}}+\frac{1}{LC}\tilde{\mathbf{D}}\tilde{\mathbf{q}}-\frac{\delta C_{\rm m}}{LC^2}\tilde{\mathbf{D}}\tilde{\mathbf{M}}\tilde{\mathbf{q}}=\frac{2}{L}\tilde{\mathbf{D}}\tilde{\mathbf{v}}^{\rm inc} \tag{53}$$

where $\tilde{\mathbf{q}}=\mathbf{U}^{\rm H}\mathbf{q}$, $\tilde{\mathbf{v}}=\mathbf{U}^{\rm H}\mathbf{v}$, $\tilde{\mathbf{D}}=\mathrm{diag}\{0,1,1\}$, and

$$\tilde{\mathbf{M}}=\frac{1}{2}\begin{pmatrix}0&e^{-i\omega_{\rm m}t}&e^{i\omega_{\rm m}t}\\e^{i\omega_{\rm m}t}&0&e^{-i\omega_{\rm m}t}\\e^{-i\omega_{\rm m}t}&e^{i\omega_{\rm m}t}&0\end{pmatrix}. \tag{54}$$

Transforming the matrix equation (53) to its constituent algebraic equations yields

$$\begin{aligned} \ddot{q}_{\rm c}+\frac{\omega_0}{Q}\dot{q}_{\rm c}&=0\\ \ddot{q}_{+}+\frac{\omega_0}{Q}\dot{q}_{+}+\omega_0^2 q_{+}-\omega_0\delta\omega_{\rm m}e^{-i\omega_{\rm m}t}q_{-}&\\ +\omega_0\delta\omega_{\rm m}e^{i\omega_{\rm m}t}q_{\rm c}&=\frac{2}{L\sqrt{3}}e^{-i\omega t}\\ \ddot{q}_{-}+\frac{\omega_0}{Q}\dot{q}_{-}+\omega_0^2 q_{-}-\omega_0\delta\omega_{\rm m}e^{i\omega_{\rm m}t}q_{+}&\\ +\omega_0\delta\omega_{\rm m}e^{-i\omega_{\rm m}t}q_{\rm c}&=\frac{2}{L\sqrt{3}}e^{-i\omega t} \end{aligned} \tag{55}$$

where $q_\pm$ are the amplitudes of the rotating states, $\omega_0=1/\sqrt{LC}$, $Q=\omega_0 L/Z_0$, and $\delta\omega_{\rm m}=\omega_0\delta C_{\rm m}/(2C)$. For the derivation of (55) we have assumed that the structure is excited from port 1 with a signal of unitary amplitude and frequency ω. The first equation in (55) shows that the common mode is not excited at all ($q_{\rm c}=0$), as deduced in the main text through first-principle arguments. Equation (55) then becomes

$$\begin{aligned} \ddot{q}_{+}+\frac{\omega_0}{Q}\dot{q}_{+}+\omega_0^2 q_{+}-\omega_0\delta\omega_{\rm m}e^{-i\omega_{\rm m}t}q_{-}&=\frac{2}{L\sqrt{3}}e^{-i\omega t}\\ \ddot{q}_{-}+\frac{\omega_0}{Q}\dot{q}_{-}+\omega_0^2 q_{-}-\omega_0\delta\omega_{\rm m}e^{i\omega_{\rm m}t}q_{+}&=\frac{2}{L\sqrt{3}}e^{-i\omega t}. \end{aligned} \tag{56}$$

Similarly to (14), (56) can be solved by making the assumption

$$\begin{aligned} q_{+}&=q_{+}^{(0)}e^{-i\omega t}+q_{+}^{(+1)}e^{-i(\omega+\omega_{\rm m})t}\\ q_{-}&=q_{-}^{(0)}e^{-i\omega t}+q_{-}^{(-1)}e^{-i(\omega-\omega_{\rm m})t} \end{aligned} \tag{57}$$

which leads to

$$\begin{aligned} q_{\pm}^{(0)}&=\frac{2}{L\sqrt{3}}\frac{\omega_0^2-(\omega\mp\omega_{\rm m})^2-i2\gamma(\omega\mp\omega_{\rm m})}{\Delta_{\mp}}\\ q_{\pm}^{(\pm1)}&=\frac{2}{L\sqrt{3}}\frac{\omega_0\delta\omega_{\rm m}}{\Delta_{\pm}} \end{aligned} \tag{58}$$

where

$$\begin{aligned} \Delta_{\pm}=\left(\omega_0^2-\omega^2-i2\gamma\omega\right)\left[\omega_0^2-(\omega\pm\omega_{\rm m})^2-i2\gamma(\omega\pm\omega_{\rm m})\right]&\\ -\omega_0^2\delta\omega_{\rm m}^2& \end{aligned} \tag{59}$$

and $\gamma=\omega_0/(2Q)$.

The S-parameters at the input frequency can be calculated as

$$\begin{aligned} S_{11}(\omega)&=1-Z_0 i_1(\omega)\\ S_{21}(\omega)&=-Z_0 i_2(\omega)\\ S_{31}(\omega)&=-Z_0 i_3(\omega) \end{aligned} \tag{60}$$

assuming $v_1^{\rm inc}=1$. Considering that $i_i(\omega)=-i\omega q_i(\omega)$ and $\mathbf{q}=\mathbf{U}\tilde{\mathbf{q}}$, (60) becomes

$$\begin{aligned} S_{11}(\omega)&=1+\frac{i\omega Z_0}{\sqrt{3}}\left[q_{+}^{(0)}+q_{-}^{(0)}\right]\\ S_{21}(\omega)&=\frac{i\omega Z_0}{\sqrt{3}}\left[q_{+}^{(0)}e^{i2\pi/3}+q_{-}^{(0)}e^{i4\pi/3}\right]\\ S_{31}(\omega)&=\frac{i\omega Z_0}{\sqrt{3}}\left[q_{+}^{(0)}e^{i4\pi/3}+q_{-}^{(0)}e^{i2\pi/3}\right] \end{aligned} \tag{61}$$

Comparing (61) with (17) and considering that for the wye resonator $d_+=\sqrt{2\gamma_{+,\rm cpl}/3}=\sqrt{2Z_0/(3L)}$, we can find that

$$a_{\pm}^{(0)}=d_{+}\frac{-i\omega\left[\omega_0^2-(\omega\mp\omega_{\rm m})^2-i2\gamma(\omega\mp\omega_{\rm m})\right]}{\Delta_{\mp}}. \tag{62}$$

If $|\omega-\omega_0|\ll\omega_0$, $\gamma\ll\omega_0$, and $\omega_{\rm m}\ll 2\omega_0$, it is possible to show that (62) simplifies to (16). Similar conclusions also hold for the modal amplitude at the intermodulation frequencies $\omega\pm\omega_{\rm m}$.

The resonances associated with the dominant sub-states of the circuit can be found from the roots of the denominator in the first equation of (58). For sufficiently high Q-factor, γ can be taken equal to 0 and

$$\omega_{\rm m\pm}=\frac{1}{2}\left[\sqrt{\omega_{\rm m}^2+4\omega_0\left(\omega_0\mp\sqrt{\omega_{\rm m}^2+\delta\omega_{\rm m}^2}\right)}\pm\omega_{\rm m}\right]. \tag{63}$$

These frequencies are shifted from ω_0 by different amounts, implying that their center of mass, $\omega_{\rm cm} = (\omega_{\rm m+} + \omega_{\rm m-})/2$, is also shifted from ω_0. In particular, it is not difficult to show that

$$\omega_{\rm cm} = \omega_0 - \frac{\omega_0}{8\omega_0^2 - 2\omega_{\rm m}^2}\delta\omega_{\rm m}^2 + O(\delta\omega_{\rm m}^4). \qquad (64)$$

Therefore, $\omega_{\rm cm}$, where isolation becomes maximum, is red shifted from ω_0 by the amount $\omega_0\delta\omega_{\rm m}^2/(8\omega_0^2 - 2\omega_{\rm m}^2)$, or, for $\omega_{\rm m} \ll \omega_0$, $\delta\omega_{\rm m}^2/(8\omega_0)$. This shifting is the result of the second-order nature of (50) and it is related to the weak coupling between positive and negative frequencies, which are completely neglected in coupled-mode analysis.

REFERENCES

[1] D. M. Pozar, *Microwave Engineering*, 3rd ed. Hoboken, NJ, USA: Wiley, 2005.

[2] L. Onsager, "Reciprocal relations in irreversible processes. I.," *Phys. Rev.*, vol. 37, pp. 405–426, Feb. 1931.

[3] H. B. G. Casimir, "On Onsager's principle of microscopic reversibility," *Rev. Mod. Phys.*, vol. 17, no. 6, pp. 343–350, Apr.–Jul. 1945.

[4] H. B. G. Casimir, "Reciprocity theorems and irreversible processes," *Proc. IEEE*, vol. 51, no. 11, pp. 1570–1573, Nov. 1963.

[5] B. Lax and K. J. Button, *Microwave Ferrites and Ferrimagnetics*. New York, NY, USA: McGraw-Hill, 1962.

[6] D. S. Gardner, G. Schrom, F. Paillet, B. Jamieson, T. Karnik, and S. Borkar, "Review of on-chip inductor structures with magnetic films," *IEEE Trans. Magn.*, vol. 45, no. 10, pp. 4760–4766, Oct. 2009.

[7] S. A. Oliver *et al.*, "Integrated self-biased hexaferrite microstrip circulators for millimeter-wavelength applications," *IEEE Trans. Microw. Theory Techn.*, vol. 49, no. 2, pp. 385–387, Feb. 2001.

[8] A. Saib, M. Darques, L. Piraux, D. Vanhoenacker-Janvier, and I. Huynen, "An unbiased integrated microstrip circulator based on magnetic nanowired substrate," *IEEE Trans. Microw. Theory Techn.*, vol. 53, no. 6, pp. 2043–2049, Jun. 2005.

[9] L.-P. Carignan, A. Yelon, D. Ménard, and C. Caloz, "Ferromagnetic nanowire metamaterials: Theory and applications," *IEEE Trans. Microw. Theory Techn.*, vol. 59, no. 10, pp. 2568–2586, Oct. 2011.

[10] S. Tanaka, N. Shimimura, and K. Ohtake, "Active circulators—The realization of circulators using transistors," *Proc. IEEE*, vol. 53, no. 3, pp. 260–267, Mar. 1965.

[11] Y. Ayasli, "Field effect transistor circulators," *IEEE Trans. Magn.*, vol. 25, no. 5, pp. 3242–3247, Sep. 1989.

[12] T. Kodera, D. L. Sounas, and C. Caloz, "Artificial Faraday rotation using a ring metamaterial structure without static magnetic field," *Appl. Phys. Lett.*, vol. 99, July 2011, Art. ID 03114.

[13] D. L. Sounas, T. Kodera, and C. Caloz, "Electromagnetic modeling of a magnetless nonreciprocal gyrotropic metasurface," *IEEE Trans. Antennas Propag.*, vol. 61, no. 1, pp. 221–231, Jan. 2013.

[14] T. Kodera, D. L. Sounas, and C. Caloz, "Magnetless nonreciprocal metamaterial (MNM) technology: Application to microwave components," *IEEE Trans. Microw. Theory Techn.*, vol. 61, no. 3, pp. 1030–1042, Mar. 2013.

[15] Z. Wang *et al.*, "Gyrotropic response in the absence of a bias field," *Proc. Nat. Acad. Sci. USA*, vol. 109, no. 33, pp. 13 194–13 197, Aug. 2012.

[16] B.-I. Popa and S. A. Cummer, "Nonreciprocal active metamaterials," *Phys. Rev. B, Condens. Matter*, vol. 85, May 2012, Art. ID 205101.

[17] K. Gallo and G. Assanto, "All-optical diode in a periodically poled lithium niobate waveguide," *Appl. Phys. Lett.*, vol. 79, no. 3, pp. 314–316, Jul. 2001.

[18] S. Manipatruni, J. T. Robinson, and M. Lipson, "Optical nonreciprocity in optomechanical structures," *Phys. Rev. Lett.*, vol. 102, May 2009, Art. ID 213903.

[19] L. Fan *et al.*, "An all-silicon passive optical diode," *Science*, vol. 335, pp. 447–450, Jan. 2012.

[20] B. Peng *et al.*, "Parity-time-symmetric whispering-gallery microcavities," *Nature Phys.*, vol. 10, pp. 394–398, May 2014.

[21] P. K. Tien and H. Suhl, "A traveling-wave ferromagnetic amplifier," *Proc. IRE*, vol. 46, no. 4, pp. 700–706, Apr. 1958.

[22] A. L. Cullen, "Theory of the travelling-wave parametric amplifier," *Proc. IEE*, vol. 107, no. 32, pp. 101–107, Mar. 1960.

[23] R. Landauer, "Parametric amplification along nonlinear transmission lines," *J. Appl. Phys.*, vol. 31, no. 3, pp. 479–484, Mar. 1960.

[24] D. Jäger and F.-J. Tegude, "Nonlinear wave propagation along periodic-loaded transmission line," *Appl. Phys.*, vol. 15, pp. 393–397, 1978.

[25] Z. Yu and S. Fan, "Complete optical isolation created by indirect interband photonic transitions," *Nature Photon.*, vol. 3, pp. 91–94, Feb. 2009.

[26] M. S. Kang, A. Butsch, and P. St. J. Russell, "Reconfigurable light-driven opto-acoustic isolators in photonic crystal fibre," *Nature Photon.*, vol. 5, pp. 549–553, Sep. 2011.

[27] X. Huang and S. Fan, "Complete all-optical silica fiber isolator via stimulated Brillouin scattering," *J. Lightw. Technol.*, vol. 29, no. 15, pp. 2267–2275, Aug. 2011.

[28] H. Lira, Z. Yu, S. Fan, and M. Lipson, "Electrically driven nonreciprocity induced by interband photonic transition on a silicon chip," *Phys. Rev. Lett.*, vol. 109, Jul. 2012, Art. ID 033901.

[29] K. Fang, Z. Yu, and S. Fan, "Photonic Aharonov–Bohm effect based on dynamic modulation," *Phys. Rev. Lett.*, vol. 108, Apr. 2012, Art. ID 153901.

[30] D.-W. Wang, H.-T. Zhou, M.-J. Guo, J.-X. Zhang, J. Evers, and S.-Y. Zhu, "Optical diode made from a moving photonic crystal," *Phys. Rev. Lett.*, vol. 110, Feb. 2013, Art. ID 093901.

[31] I. K. Hwang, S. H. Yun, and B. Y. Kim, "All-fiber-optic nonreciprocal modulator," *Opt. Lett.*, vol. 22, no. 8, pp. 507–509, Apr. 1997.

[32] C. R. Doerr, N. Dupuis, and L. Zhang, "Optical isolator using two tandem phase modulators," *Opt. Lett.*, vol. 36, no. 21, pp. 4293–4295, Nov. 2011.

[33] C. Galland, R. Ding, N. C. Harris, T. Baehr-Jones, and M. Hochberg, "Broadband on-chip optical non-reciprocity using phase modulators," *Opt. Exp.*, vol. 21, no. 12, pp. 14 500–14 511, Jun. 2013.

[34] S. Qin, Q. Xu, and Y. E. Wang, "Nonreciprocal components with distributedly modulated capacitors," *IEEE Trans. Microw. Theory Techn.*, vol. 62, no. 10, pp. 2260–2272, Oct. 2014.

[35] D. L. Sounas, C. Caloz, and A. Alù, "Giant non-reciprocity at the subwavelength scale using angular momentum-biased metamaterials," *Nat. Commun.*, vol. 4, Sep. 2013, Art. ID 2407.

[36] R. Fleury, D. L. Sounas, C. F. Sieck, M. R. Haberman, and A. Alù, "Sound isolation and giant linear nonreciprocity in a compact acoustic circulator," *Science*, vol. 343, pp. 516–519, Jan. 2014.

[37] D. L. Sounas and A. Alù, "Angular-momentum-biased nanorings to realize magnetic-free integrated optical isolation," *ACS Photon.*, vol. 1, pp. 198–204, 2014.

[38] N. A. Estep, D. L. Sounas, J. Soric, and A. Alù, "Magnetic-free non-reciprocity and isolation based on parametrically modulated coupled-resonator loops," *Nature Phys.*, vol. 10, pp. 923–927, Dec. 2014.

[39] N. A. Estep, D. L. Sounas, and A. Alù, "Angular-momentum-biasing for non-reciprocal electromagnetic devices," in *Wireless Microw. Circuits Syst. Symp.*, Waco, TX, USA, Apr. 3–4, 2014, pp. 1–4.

[40] N. A. Estep, D. L. Sounas, and A. Alù, "On-chip non-reciprocal components based on angular-momentum biasing," in *IEEE MTT-S Int. Microw. Symp. Dig.*, Phoenix, AZ, USA, May 17–22, 2015, pp. 1–4.

[41] W. Suh, Z. Wang, and S. Fan, "Temporal coupled-mode theory and the presence of non-orthogonal modes in lossless multimode cavities," *IEEE J. Quant. Electron.*, vol. 40, no. 10, pp. 1511–1518, Oct. 2004.

[42] J. Helszajn, *The Stripline Circulator: Theory and Practice*. New York, NY, USA: Wiley, 2008.

[43] K. Buisman *et al.*, "Distortion-free varactor diode topologies for RF adaptivity," in *IEEE MTT-S Int. Microw. Symp. Dig.*, Long Beach, CA, USA, Jun. 12–17, 2005.

[44] D. J. Griffiths, *Introduction to Quantum Mechanics*. Upper Saddle River, NJ, USA: Prentice-Hall, 1995.

Nicholas Aaron Estep received the B.S. degree in electrical engineering from The University of Texas at Austin, Austin, TX, USA, in 2006, the M.S. degree in electrical engineering from the Air Force Institute of Technology, Dayton, OH, USA, in 2010, and is currently working toward the Ph.D. degree in electrical engineering at The University of Texas at Austin.

His research interests include metamaterials and plasmonics, nonreciprocal electromagnetic devices, and electromagnetic propagation in dispersive, bi-anisotropic media.

Dimitrios L. Sounas (M'11) received the Diploma/ M.Eng. and Ph.D. degrees in electrical and computer engineering (with highest honors) from the Aristotle University of Thessaloniki, Thessaloniki, Greece, in 2004 and 2009, respectively.

From August 2010 to October 2012, he was a Post-Doctoral Fellow with the Electromagnetic Theory and Applications Research Group, École Polytechnique de Montréal. Since November 2012, he has been a Post-Doctoral Fellow with the Metamaterials and Plasmonics Research Group, The University of Texas at Austin, Austin, TX, USA. He has authored or coauthored over 40 journal papers, 70 conference papers, and 2 book chapters, among which include papers in highly selective journals including *Science*, *Nature Physics*, *Nature Communications*, *Physical Review Letters*, and IEEE TRANSACTIONS. He holds and four patents. His research interests span over a broad range of areas including electromagnetis, optics, metamaterials, plasmonics, nonreciprocity, spatiotemporal modulation, parity-time symmetry, and graphene. He has made major contributions in the area of magnetless nonreciprocal components, which attracted significant interest from public media and telecommunications industry for inclusion in next-generation wireless communication systems.

Andrea Alù (S'03–M'07–SM'12–F'14) received the Laurea, M.S., and Ph.D. degrees from the University of Roma Tre, Rome, Italy, in 2001, 2003, and 2007, respectively.

He is currently an Associate Professor and David & Doris Lybarger Endowed Faculty Fellow in Engineering with The University of Texas at Austin, Austin, TX, USA. From 2002 to 2008, he has periodically worked with the University of Pennsylvania, Philadelphia, PA, USA, where he has also developed significant parts of his doctoral and postgraduate research. After spending one year as a Postdoctoral Research Fellow with the University of Pennsylvania, in 2009 he joined the faculty of The University of Texas at Austin. He is also a member of the Applied Research Laboratories and of the Wireless Networking and Communicaions Group, The University of Texas at Austin. He has coauthored an edited book on optical antennas, over 250 journal papers, and over 20 book chapters. His current research interests span over a broad range of areas including metamaterials and plasmonics, electromangetics, optics and photonics, scattering, cloaking and transparency, nanocircuit and nanostructure modeling, miniaturized antennas and nanoantennas, and RF antennas and circuits.

Dr. Alù is a full Member of URSI. He is a Fellow of the Optical Society of America (OSA) and the American Physical Society (APS). He is a Senior Member of SPIE. He is a Member of MRS. He has organized and chaired various special sessions in international symposia and conferences. He is currently on the Editorial Board of *Physical Review B*, *Scientific Reports* and *Advanced Optical Materials*. He serves as an Associate Editor for four journals including IEEE ANTENNAS AND WIRELESS PROPAGATION LETTERS and *Optics Express*. He has been the Guest Editor for Special Issues of the IEEE JOURNAL OF SELECTED TOPICS IN QUANTUM ELECTRONICS, *Optics Communications*, *Metamaterials*, and *Sensors* on a variety of topics involving metamaterials, plasmonics, optics, and electromagnetic theory. He has served as an OSA Traveling Lecturer since 2010, and IEEE AP-S Distinguished Lecturer since 2014, and as the IEEE joint AP-S and Microwave Theory and Techniques Society (MTT-S) Chapter for Central Texas. He was the recipient of several research awards including the NSF Alan T. Waterman Award (2015), the OSA Adolph Lomb Medal (2013), the IUPAP Young Scientist Prize in Optics (2013), the IEEE MTT-S Outstanding Young Engineer Award (2014), the Franco Strazzabosco Award for Young Engineers (2013), the URSI Issac Koga Gold Medal (2011), the SPIE Early Career Investigator Award (2012), an National Science Foundation (NSF) CAREER Award (2010), the Air Force Office of Scientific Research (AFOSR) and the Defense Threat Reduction Agency (DTRA) Young Investigator Award (2010 and 2011), and Young Scientist Award from the URSI General Assembly (2005) and URSI Commission B (2010, 2007, and 2004). His students have also been the recipient of several awards including the Student Paper Award of the IEEE Antennas and Propagation Symposia (2011 and 2012).